SYNTHESIS AND CHARACTERIZATION OF FASnI$_2$Br AND ZnO:S FOR FABRICATION OF ENHANCED-EFFICIENCY PEROVSKITE SOLAR CELLS

CEPHAS ROHN ODHIAMBO

A Thesis Submitted to the Graduate School in Partial Fulfilment of the Requirement for Master of Science Degree in Physics of Egerton University

EGERTON UNIVERSITY

JULY, 2025

DECLARATION AND RECOMMENDATION

Declaration

This thesis is my original work and has not been presented in this university or any other for the award of a degree

Signature...….. Date…July 07/2025……………

Cephas Rohn Odhiambo

SM13/13097/21

Recommendation

This thesis has been submitted with our approval as University supervisors.

Signature… Date…July 07, 2025………………

Dr. Duke Oeba, PhD
Department of Physics
Egerton University

Signature… Date…July 07/2025………………

Dr Jared Ombiro, PhD
Department of Mathematical and Physical Sciences
Maasai Mara University

COPY RIGHT

DEDICATION

I dedicate this thesis to my lovely parents Sabastian Cephas Akumu and Elizabeth Auma Cephas, my Siblings Joan, Violet, Kenroset, Faith, Prince, Vastine, Tayrine and Christian. I also dedicate it to all my friends who inspired me throughout my academic journey.

ACKNOWLEDGEMENTS

Most importantly, I deeply express my gratitude to almighty God for the life, knowledge and wisdom He has given me to do Master of Science in Physics degree and to successfully carry out my research project. Secondly, I am full of gratitude to Egerton University for my admission to pursue Masters of Science in Physics through the Board of postgraduate studies. This was a wonderful learning experience. Similarly, I am grateful to (United Nations Educational, Scientific and Cultural Organization in conjunction with the World Academy of Sciences for the advancement of science in developing countries (UNESCO- TWAS) for paying my school fees and funding my project. This was done through Dr Duke Oeba who was awarded Seed Grant for New African Principal Investigators of Research grant number 4500474973.

Thirdly, I sincerely am sincerely grateful Dr Duke Oeba, my supervisor from Physics department for his guidance, supervision, financial support, constant encouragement and pieces of advice throughout the research project period. Thank you also for choosing me among many students for the UNESCO-TWAS award. In the same way, I am grateful to Dr Jared Ombiro; Department of Mathematical and Physical Sciences of Maasai Mara University for his outstanding support, supervision and guidance during my research project. In addition, I would like appreciate my technical supervisor Mr. Fred Mukwa for his supervision, guidance and advice during the project. I also thank all academic and technical staff in Physics department of Egerton University for their support, inspiration and guidance during my coursework and research project. Besides, I sincerely appreciate all my colleagues for all their inputs during my studies.

Lastly, I thank my parents Mr. and Mrs. Sabastian Cephas for their financial support, encouragement, prayers, counsel and inspiration. May God bless everyone who supported me.

ABSTRACT

Clean and renewable energy sources have experienced significant demand in recent years due to their necessity for sustainable industrial development. This requirement is also emphasized by the United Nations' Sustainable Development Goal 7, "Affordable and Clean Energy." The advent of perovskite solar cells has generated considerable interest in the energy sector, offering hope for advancements in solar technology. Perovskite solar cells are known for their high efficiency and ability to convert a wide range of light wavelengths into electricity. Additionally, these solar cells exhibit excellent charge carrier mobility, light absorption and have a high tolerance for structural defects. However, perovskite solar cells face challenges related to toxicity and instability. This research addressed these issues by investigating lead free $FASnI_2Br$. Furthermore, incorporating bromine into $FASnI_3$ and sulphur into ZnO was aimed at enhancing the stability solar cells fabricated with these materials. This approach improved thermal stability, resulting in a well-ordered, compact crystal lattice and reducing the propensity for phase transitions or degradation at higher temperatures. It also enhanced moisture stability through defect passivation. In this study, $FASnI_2Br$ and ZnO:S suitable for perovskite device applications was synthesized by spin coating using solution-based technique. Structural and optoelectronic characterization was performed using X-ray diffraction (XRD) and ultraviolet-visible (UV-Vis) spectroscopy, respectively. The ZnO:S was observed to show wurtzite hexagonal structure that agrees with theoretical information. Finally, perovskite solar cells were fabricated on indium-doped tin oxide glass substrates using a spin coater. Doping enhanced the transmission through ZnO:S making it best suited as an electron transport layer (ETL) material. For $FASnI_2Br$, the XRD structure exhibited peaks of a perovskite material. The doping increased optical absorption of $FASnI_3$ making it best suited for perovskite material. A power conversion efficiency (PCE) of 16.5%, Jsc of 21.3 $mAcm^{-2}$ and Voc of 1.15 V were obtained using ZnO:S ETL tested with $FAPbI_3$. The solar cell fabricated with $FASnI_2Br$ exhibited moderate performance and favourable electrical properties; PCE of 3.57%, Voc of 0.569 V and Jsc of 0.568 $mAcm^{-2}$. It was also concluded that ZnO: 4%S performed better than ZnO: 8%S doping concentrations. This research significantly contributes to the field by developing non-toxic, stable materials for perovskite solar cells. The enhanced performance can still be achieved by studying interfacial layer materials as well as passivation materials. This will in future, revolutionize photovoltaic technology, paving the way for more efficient and durable solar energy solutions.

TABLE OF CONTENTS

LIST FIGURES

LIST OF ABBREVIATIONS AND ACRONYMS

CdS	Cadmium sulphide
DSSCs	Dye-Sensitized Solar Cells
ETL	Electron Transport Layer
HTL	Hole Transport Layer
ITO	Indium Tin Oxide
PEDOT: PSS	Poly (3,4-ethylene dioxythiophene): poly (styrene sulfonate)
PSCs	Perovskite Solar Cells
PTAA	poly[bis(4-phenyl) (2,4,6-trimethylphenyl) amine
PV	Photovoltaic technology
TBP	4-tert-butylpyridine
TBT	(Tetrasubstituted Thieno[3,2-b] thiophenes)
UV	Ultra Violet

LIST OF SYMBOLS

ABX_3	A and B are cations of different sizes and X is an anion
λ	Wavelength

CHAPTER ONE

INTRODUCTION

1.1 Background Information

There is a great demand for clean and renewable energy sources for sustainable industrial development. This is due to the exhaustion of fossil fuels, the major non-renewable energy extracted from coal, petroleum, and natural gas (Wang *et al.*, 2019). This demand is also confirmed by the 7th sustainable development goal of the United Nations, “Affordable and Clean Energy” (Katila *et al.*, 2019). Renewable energy sources include wind, nuclear, biomass, geothermal, hydroelectricity, and solar energy. However, the advantages of solar energy supersede all of these renewable energy sources. Wind energy requires a larger space, has noise pollution as the turbines rotate, and the rotations of turbines may be dangerous to some wildlife, such as birds (Wang & Wang, 2015). Nuclear energy faces challenges such as high construction costs for nuclear plants, health and safety risks, political implications and conflict vulnerability, and production of radioactive waste products, making it inconvenient as a renewable energy source (Yuksel *et al.*, 2021). Biomass is not entirely clean, can lead to deforestation, and is less efficient than fossil fuels (Madriaga *et al.*, 2023). Hydroelectric power has some adverse environmental impact, is expensive up-front, requires reservoirs, and relies on local hydrology (Baird *et al.*, 2021). Geothermal energy is expensive to sustain, may encourage earthquakes, and has environmental side effects like pollution (Zheng *et al.*, 2015). On the other hand, solar energy is both renewable and clean, remains green until the end of life, there is a lot of technological development in solar energy area, requires minimum maintenance, experienced everywhere, and has the ability to create wealth and jobs locally (Stevanović *et al.*, 2022). For these reasons, solar energy has become the most favourable energy source in the world today. However, its full potential has not been fully explored.

Scientific research on solar energy has led to solar cell developments, currently classified into four generations as illustrated in Figure 1.1. These include first-generation, second-generation, third-generation, and the latest fourth-generation solar cell technology (Chawla *et al.*, 2020). The first-generation solar cells are mainly silicon-based, made of either monocrystalline or polycrystalline silicon wafers (Chawla *et al.*, 2020). The major limitations of silicon-based solar cells are the higher risk of reducing efficiency at very high temperatures and the high initial cost (Milichko *et al.,* 2016; Olaleru *et al.*, 2020). Due to these shortcomings, continual research gave birth to second-generation solar cells characterized by developing thin film photovoltaic cells from amorphous silicon, cadmium telluride or sulfide, gallium arsenide, and copper indium gallium (Chawla *et al.*, 2020). The shortcomings of the second-generation PV technology such as low efficiency, fast degradation by light, and inadequate raw materials, necessitated the development of third-generation solar cells (Milichko *et al.,* 2016; Olaleru *et al*., 2020). The third-generation solar cells are majorly dye-sensitized solar cells. Others include copper zinc tin sulfide (CZTS) and organic solar cells (Chawla *et al*., 2020). The main limitations of the third generation include using liquid electrolytes, temperature stability problems in dye-sensitized solar cells (DSSC), and surface defects leading to the recombination of holes and electrons (Milichko *et al.,* 2016; Olaleru *et al*., 2020). Further research led to the development of fourth-generation solar cells characterized by quantum dots, and perovskite solar cells (Chawla *et al*., 2020; Kant & Singh, 2022). It's characterized by nanomaterials, quantum dots, and perovskites solar cells (PSCs).

The major advantages of perovskites solar include their ability to react with various wavelengths of light thus converting more light into electricity, are highly efficient and can compete favorably with silicon-based solar cells, and have great tolerance to defects of structure as opposed to silicon-based. Lastly, these solar cells have excellent charge carrier mobility, light absorption, and lifetimes (Mohammed *et al*., 2020). The major types of Inkjet printing of perovskite solar cells are organic metal halide perovskites, inorganic oxide perovskites, and alkaline metal halide Perovskites. Figure 1.1 illustrate the renewable or green energy sources and generations of solar cells.

The working principle of perovskite solar cells is that as light falls on the perovskite layer (absorber layer), it is absorbed, and excitons are generated. Electrons and holes are simultaneously created by the absorbed light energy and are separated into different contacts. Electrons move to the anode while holes move into the cathode. External gadgets or loads can therefore be connected through it. Perovskite solar cells will likely overtake other solar technologies due to the advantages described in the previous paragraph. For example, their power conversion efficiencies (PCEs) have reportedly been on the rise since 2009 of 3.8 % (Zhou *et al*., 2018). In 2016, for example, a PCE of 23.3 % was obtained, improved to 25.2 % by the same year (Akman *et al*., 2021; Dai *et al*., 2021) and has indicated an increase in the recent past, with the latest captured being 31.57 % through SCAPS-1D method (Mattaparthi *et al*., 2023). However, despite the success of perovskites solar cell, it is faced with problem of toxicity and instability. The toxicity problem is because lead has been listed among the top toxic metals with ability to cause high blood pressure, brain, kidney and reproductive health issues when inhaled, or when it enters the body through other means such as drinking water. A lot of researches have been put forward in solving the problem of toxicity. Generally, lead free perovskite solar cells fabricated using metals such as tin, antimony, and bismuth as well as using halide double perovskite has been investigated and researched. Currently, tin-based perovskite solar cells is the leading metal researched for lead free.

Figure 1.1: Schematic diagram for green energy with solar cell generations

On the other hand, the problem of stability is also under research with some solutions put in place include use of formamidinium based perovskite material instead of methyl ammonium based and methyl ammonium based with mixed halide perovskite material. Nevertheless, to the best of my knowledge, the effect of mixed halide in the formamidinium perovskite material on performance has never been investigated.

1.2 Statement of the Problem

One of the world's major problem today is inadequate clean and renewable energy, which has led to pollution and global warming brought about by overreliance on fossil fuels. The effects of global warming have further resulted in the encroachment of drought, thus negatively impacting the general population. Therefore, for sustainable development, as captured by the United Nations Sustainable Development Goal number 7, that is affordable and sustainable, clean energy is a major requirement. Different generations of solar cells, such as first-generation, second-generation, and third-generation, have been developed to address this problem. However, all of these generations of solar cells are faced with limitations, thus discouraging their application. The recent perovskite solar cells are sources of hope for these problems. However, despite the positive trend in efficiency, perovskite solar cells are faced with problems of toxicity and instability. For this reason, other materials like tin, antimony, and bismuth as well as using halide double perovskite, have been put in place. This research was intended to improve the performance of lead-free perovskites solar cells, which are environmentally friendly, stable, and economical.

1.3 Objectives

1.3.1 General Objective

To synthesize and characterize the materials $FASnI_2Br$ and ZnO:S and to evaluate their effectiveness in improving the efficiency and stability of perovskite solar cells.

1.3.2 Specific Objectives

i. To synthesize $FASnI_2Br$ and ZnO:S materials using solution-based technique for application in perovskite solar device.
ii. To investigate the structural properties of $FASnI_2Br$ and ZnO:S using X-ray diffraction.
iii. To determine the optical properties of $FASnI_2Br$ and ZnO:S using UV-Vis spectroscopy.
iv. To fabricate and characterize the perovskite solar cells using $FASnI_2Br$ and ZnO:S.

1.4 Research Questions

i. Can solution-based method be used to synthesize $FASnI_2Br$ and ZnO:S for application in perovskite solar cell device?
ii. What are the crystal structures of $FASnI_2Br$ and ZnO:S as determined by X-ray diffraction?
iii. What are the optical properties of $FASnI_2Br$ and ZnO:S as determined by UV-Vis spectroscopy?
iv. How do perovskite solar cells fabricated with $FASnI_2Br$ and ZnO:S perform in terms of key photovoltaic metrics such as power conversion efficiency, fill factor, open circuit voltage and short circuit current density.

1.5 Justification

The global demand for clean and renewable energy sources is growing rapidly due to the need for sustainable industrial development and environmental conservation. Solar energy, as a clean and abundant resource, plays a crucial role in meeting these energy demands. Perovskite solar cells have emerged as a promising technology in the field of photovoltaic due to their high efficiency and potential for low-cost production. However, two significant challenges hinder their widespread adoption: toxicity and instability. Traditional perovskite solar cells commonly use lead-based materials, which pose environmental and health hazards. By synthesizing and characterizing $FASnI_2Br$ (a tin-based perovskite material), this research aims to address the toxicity issue, providing a safer alternative to lead-based compounds. Tin-based perovskites are less toxic and offer a viable path toward environmentally friendly solar cells. Stability remains a critical challenge for perovskite solar cells, which are prone to degradation under thermal and moisture conditions. Incorporating bromine into $FASnI_3$ and sulphur into ZnO was for to enhancement the thermal and moisture stability of the perovskite structure. The research involved structural and optoelectronic characterization of the synthesized materials using X-ray diffraction (XRD) and UV-Vis spectroscopy. These characterization techniques confirmed the structural integrity and optoelectronic properties of $FASnI_2Br$ and ZnO ensuring that the requirements for high-performance solar cells are met. The study also culminated in the fabrication of perovskite solar cells using the newly synthesized materials. By optimizing the fabrication process and integrating $FASnI_2Br$ as the active layer and ZnO as the electron transport layer, the research aimed to achieve significant improvements in the efficiency and stability of perovskite solar cells. This research offered substantial scientific contributions by developing and characterizing new materials that address the toxicity and stability issues in perovskite solar cells. Ultimately, this study contributed to the advancement of sustainable energy technologies, aligning with global efforts to provide affordable and clean energy solutions.

CHAPTER TWO

LITERATURE REVIEW

2.1 Crystal and Electronic Structure of Perovskites

Perovskite solar cells use perovskite-structured light absorbers for their photovoltaic work (conversion of sunlight into electricity). Perovskite absorbers have a general formula of ABX_3 where both A and B are cations of different sizes and X is an anion. A is a very large cation that is either organic or inorganic such as methyl ammonium, $CH_3NH_3^+$ (MA^+), or formamidinium $CH(NH_2)_2^+$ (FA^+), and is located at the apex of the face-centred cubic lattice (Coulibaly *et al*., 2019). Group B is a small inorganic cation such as Cu^{2+}, $Pb^{2+,}$ and Sn^{2+} while X is an anion that can bond with A and B and is mostly a halide such as Cl^-, $Br^{-,}$ and I^-. The sample structure of a basic perovskite compound of the unit cell is shown in Figure 2.1. The common light absorbers are methyl –ammonium-lead-iodide ($MAPbI_3$) and formamidium-lead-iodide ($FAPbI_3$) (Akman *et al*., 2021; Bonadio *et al*., 2021; Dai *et al*., 2021; Park *et al*., 2020; Shalan *et al*., 2020; Wang *et al*., 2021; Yoo *et al*., 2021). Chloride mixed with Iodide halide perovskite ($MAPbI_{3-y}Cl_y$) is used since the mixture is stable for temperatures more than 140 °C and is a better charge carrier than Methyl-ammonium lead iodide ($MAPbI_3$).

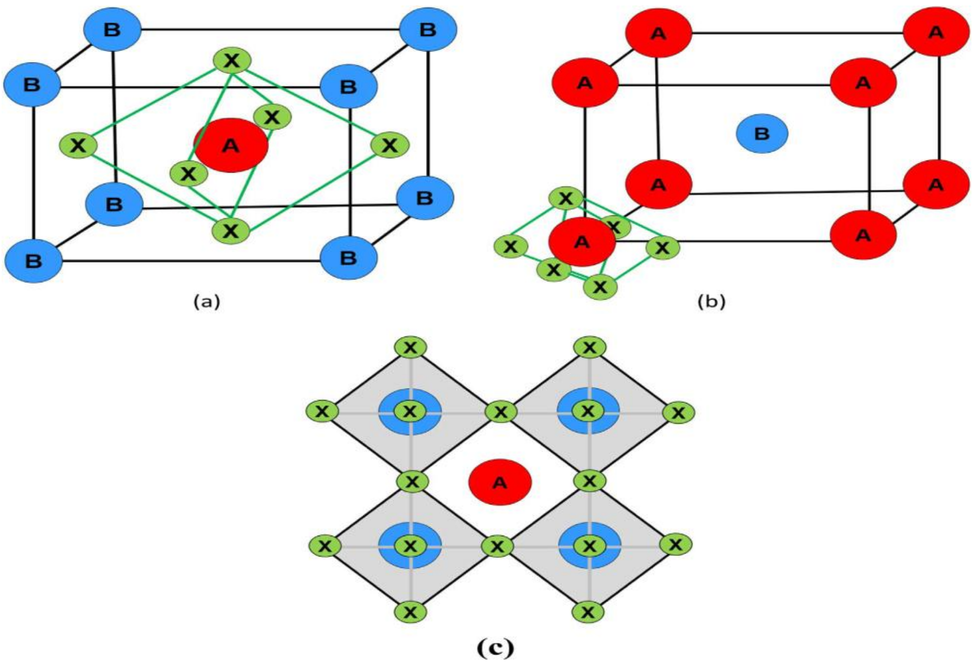

Figure 2.1: Unit cell of ABX_3 (a) Atom B is at the position <0,0,0>, (b) Atom A is at <0,0,0> position, and (c) the bonds B-X are represented in octahedral shape (BX_6)

Source: Asghar *et al*. (2017)

In recent days, perovskite solar cells made of lead halide have attracted a lot of research due to their simple techniques of processing and their cost being lower than silicon solar cells (Sung *et al.*, 2015; Du *et al.*, 2016). Despite meaningful progress, the toxicity of lead is a major challenge that is still under research on PSCs, thus demanding a search for an alternative environmentally friendly candidate instead of lead that has an appreciable efficiency (Kanoun *et al.*, 2019). From past studies, it has been observed that tin halide of a narrow bandgap of 1.3eV is a suitable replacement for lead halide since it has a wider range of visible light spectrum than that of lead (Konstantakou & Stergiopoulos, 2017).

In this research work, $FASnI_2Br$ will be used as a perovskite absorber layer. Incorporation of chlorine into $FASnI_3$ improves the stability by enhancing thermal stability. The chlorine leads to a well-ordered and compact crystal lattice and decreasing phase transition propensity or degradation that occurs at higher temperatures often above 100 °C (Chen & Dhakal, 2023). Moreover, bromine will modify the band gap of $FASnI_3$ thus enabling its compatibility with other solar materials. Similarly, bromine enhances moisture resistance by passivation defects and thus serves as a pathway for the penetration of moisture and less degradation in humid air (Esmaeili & Khosroabadi, 2021).

2.2 Perovskites Solar Cell Structure

Normal perovskite solar cells consist of three major layers; a hole transport layer (HTL), a perovskite absorber layer, and an electron transport layer (ETL). These regions exist between back contact electrodes and front contact electrodes as shown in Figure 2.2. Where Figure 2.2 a) shows n-i-p structure and b) shows p-i-n structure (Kanoun, *et al.*, 2019; Roy *et al.*, 2022).

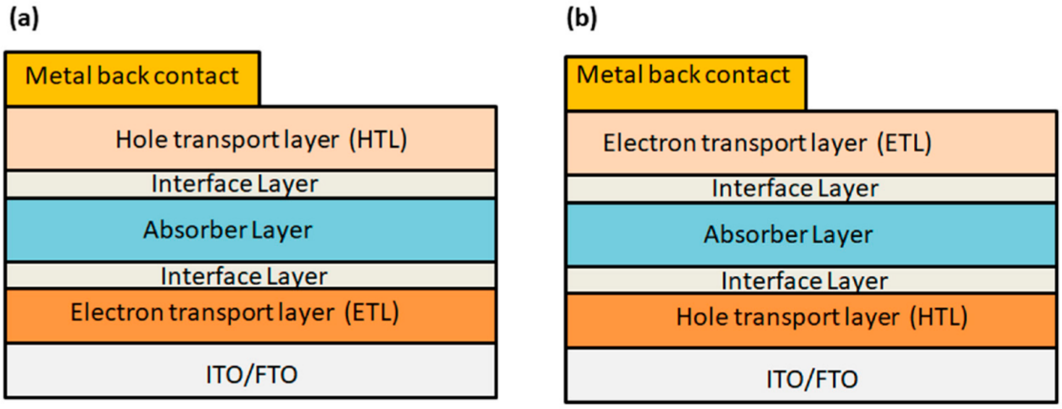

Figure 2.2: Structure of perovskite solar cell (a) n-i-p structure, (b) p-i-n structure

Source: Roy *et al.* (2022)

The solar cell radiation is absorbed by the perovskite compound thus generating charge carriers; holes, and electrons. The HTL and ETL then permit a specific number of charge carriers to penetrate the electrodes depending on the HTL and ETL materials (Kanoun *et al.*, 2019; Wang *et al*., 2019).

2.2.1 Contact Electrode Materials

Contact electrodes are situated at the top and the bottom of the PSCs and are part of the solar cells exposed to the environment. Thus, the contacts are prone to degradation. The material used must therefore remain chemically and thermally stable and should be able to lower the penetration of moisture into the perovskite layer. Electrodes are very important for the long-term operation of perovskite solar cells. Silver (Ag) and gold (Au) are the most common materials used to make the top electrode. However, silver mostly reacts with the halides forming silver halides, leading to cell degradation (Kato *et al.,* 2015). For example, it reacts with chlorine and iodine to give silver chloride and silver iodide, respectively. The formation of the two halides further causes short-circuiting or shunting leading to the degrading of the PSCs. Gold electrodes are more stable and are thus preferred over silver (Calado *et al.,*2016; Guanera *et al.,* 2015). On the other hand, some reports insinuate that if gold diffuses into the perovskite layer, it can cause permanent degradation (Domanski *et al.*, 2016). To protect the metal electrodes, better oxides are used to protect the corrosion of the halide. Other contact electrode materials include platinum, nickel, carbon, etc. In the case of this work, silver electrode was used due to its low impedance, low toxicity in comparison to calomel electrode.

2.2.2 Hole Transport Layer (HTL)

The HTL plays an important role in hole transportation and deceleration of charge recombination. The stability of the perovskite layer also depends on the morphology, the hydrophobic property of the HTL, and the interphase between the Perovskite layer and HTL (Leijtens *et al*., 2017). Spiro-OMeTAD is the most commonly used HTL, and the dopants including Lithium salt (Li-TFSL) and Bis(trifluoromethane)sulfonamide for boosting the polarity thus stimulating hole mobility and hence achieving improved interfacial contact between the perovskite layer and HTL (Calado *et al.,* 2016). TBT (*Tetrasubstituted Thieno[3,2-b] thiophenes)* can also be used, but on the contrary, it dissolves the perovskite and for this reason is avoided. The addition of buffer solution such as Al_2O_3, MoOx (molybdenum oxide), graphene oxide, and tetra-n-butyl-copper thiocyanate at HTM and perovskite interface reduces degradation (Chen *et al.*, 2016). The possible organic alternatives with high charge mobilities include poly(triaryl amine) (PTAA), poly[9-(1-octylnonyl)-9H-carbazole-2-7diyl]-2,5-thiophenediyl-2,1,3-benzothiodiazole-4-7diyl-2-5thiophenediyl](PCDTBT), poly3,4ethylenedioxythiophene:polystyrenesulfonate(PEDOT:PSS), poly[N-9-heptadecanyl-2,7-carbozole-alt-3,6-bis(thiophen-5-yl)-2-5-dioctyl-2,5-dihydropyrrolo[3,4]pyrrole-1,4dione (PCBTDPP) and etc.

2.2.3 Electron Transport Layer (ETL)

The role of ETL is to transmit light-generated electrons to the anode from the perovskite layer. The most common material used in ETL is titanium dioxide (TiO_2) owing to its non-toxicity, its good electrical properties as well as its chemical stability. On the negative side, it adsorbs oxygen, thus leading to the degradation of the perovskite layer when exposed to ultraviolet radiation (Kumar *et al.*, 2020). Additionally, TiO_2 also shows low electron mobility does not support PSCs on flexible substrates, and requires a very high temperature of 500°C for synthesis. Due to these shortcomings, inorganic metal oxides are used as substitutes and include zinc sulphide (ZnS), tin oxide (SnO_2) and cadmium sulphide (CdS) (Chen & Tseng, 2017; Jia *et al.*, 2018). Zinc oxide is a better alternative due to its good properties such as a band gap of 3.2eV, very high electron mobility of $200cm^2V^{-1}s^{-1}$ above that of TiO_2 which enables the extraction of electrons, low cost as compared to TiO_2 due to its lower temperature of crystallization and high durability (Abidin *et al*., 2023).

For this research, sulphur doped ZnO ETL was synthesized and used. The purpose for doping was for enhancing chemical stability, band gap engineering or band gap tunabilty, its compatible to many solar cell materials and modification of charge carriers (Li *et al*., 2021).

2.3 Stability of Perovskites Solar Cells

2.3.1 Factors Affecting the Stability of Perovskite Solar Cells

The stability of the PSCs is affected by factors such as temperature, fabrication method, material used, oxygen, and water or moisture as shown in Figure 2.3 (Beygisangchin, *et al.*, 2024). To begin with thermal instability or temperature, the effects are observed both at high and low temperatures. At low annealing temperatures, there is a major impact on the perovskite film morphology, photovoltaic performance as well and stability (Wu *et al.*, 2024). From prior investigations, it has been found that a least temperature of 80°C is needed to change PbI_2 and MAI to $MAPbI_3$ and a further increase in temperature will lead to the change in morphology as well as the formation layer of crystalline particles on the mesoporous TiO_2 film substrate surface. At increasing temperatures, there is degradation of $MAPbI_3$ material due to deposition of PbI_2 (Shahbazi & Wang, 2016).

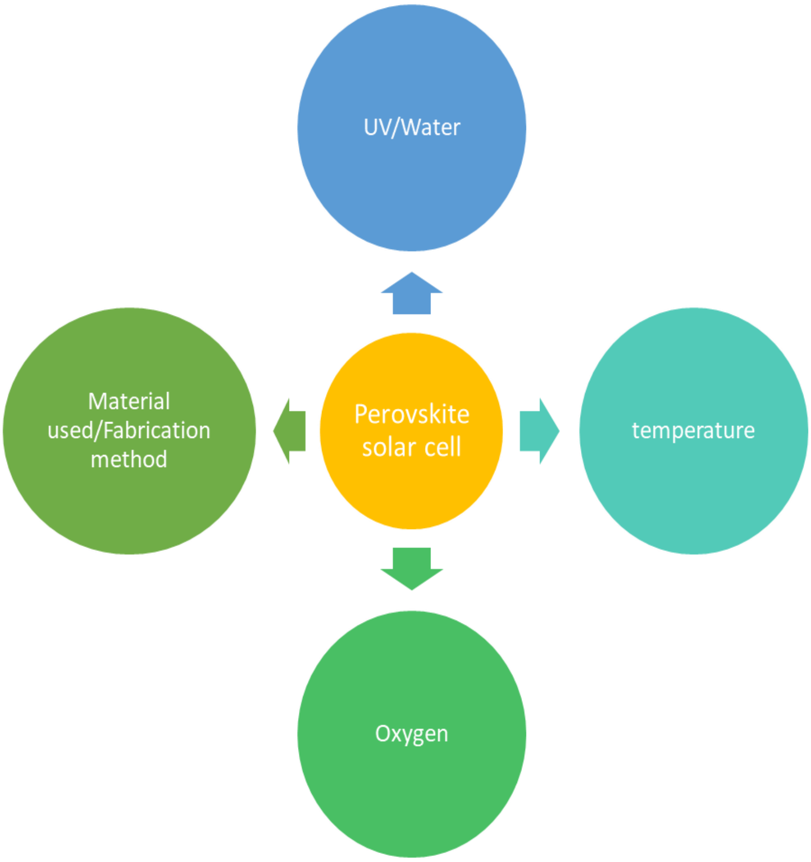

Figure 2.3: Factors affecting the stability of perovskite solar cells

Due to thermal annealing, $MAPbI_{3-x}Cl_x$ can also undergo three stages which include: At room temperature, there is a crystalline precursor of the structure, at medium temperature below 120°C there is perovskite structure and degradation due to the presence of a mixture of compounds (PbI_2) at higher temperature the transition between these three stages depends on both environmental temperature, annealing temperature as well as the film thickness (Tan *et al*., 2014). Moreover, heating $MAPbI_3$ in vacuum can change the band gap from 1.5eV for a temperature less than 140°C and to 2.36eV for a temperature greater than 140°C. (Shahbazi & Wang, 2016; Wei *et al*., 2014).

Secondly, UV affects the stability of the PSCs. It was observed that there is a formation of metallic lead on irradiation of UV in PbX_2 (Leijtens *et al*., 2013). For this reason, it is necessary to investigate the general behavior of the photo-generated charge carriers which are sometimes transported by mesoporous TiO_2 layers. The degradation due to UV is also explained by the fact that in TiO_2, there are many oxygen-free spaces or holes (p-type) and electrons (n-type) charge carriers. The electrons from TiO_2 combine with holes from oxygen thus degradation (Leijtens *et al.*, 2013). The photostability is affected by crystals' spatial arrangement and fluorinated perovskite reduces UV-influenced oxidation (Wei *et al.,* 2014).

Thirdly, the fabrication method is also a major factor affecting the stability of PSCs. The method of blade coating affects the stability and performance of the photovoltaic PSCs with planar structures. In comparison, the perovskite films prepared by spin coating and doctor blading illustrated that the reduced photovoltaic performance is brought by the degradation of perovskite materials (Yu *et al.,* 2017).

Lastly, water vapour has been observed as a factor influencing the stability of perovskite solar cell. High polarity in water from the atmosphere is able to change the structure of the perovskite solar cell. For example, methyl ammonium lead iodide in the presence of water can decompose to methyl ammonium iodide and lead iodide and thus making the perovskite layer unstable as illustrated in Rxn 2.1 (Li & Liu, 2017).

$$\mathrm{MAPbI_3} \overset{H2O}{\longleftrightarrow} MA\mathrm{I} + \mathrm{PbI_2} \qquad \text{Rxn 2.1}$$

Fourthly, oxygen effects the stability of the PSCs. Oxidation of tin as well as lead in tin-based PSCs and lead-based PSCs causes a major problem of instability. However tin results in a greater problem than lead since Sn^{2+}/Sn^{4+} has a lower redox potential of +0.15V which is below that of lead of +1.67V for Pb^{2+}/Pb^{4+} and for that reason, lead is more stable than tin. Therefore, when the Sn^{2+} ion is exposed to the ambient conditions, it results in oxidation, which releases charge thus destroying the neutrality of the perovskite layer. As a result, $FASnI_3$ and $MASnI_3$ decompose bringing about changes in electronic properties including diffusion length, conductivity, charge mobility, and alignment of the band gap. (Aftab & Ahmad, 2021; Gupta *et al.,* 2018). It is therefore obvious that Sn^{2+} and Sn^{4+} lead to the creation of extra holes rendering it positive since holes are p-type charge carriers (Aftab & Ahmad, 2021; Gupta *et al.*, 2018). Due to the toxicity of lead and the desire to ensure safety of the solar cell, the research will use tin-based perovskite layer ($FASnI_2Br$ and minimize the oxidation of tin by introduction of bromine into $FASnI_3$.

2.3.2 Improving the Stability of the Perovskite Solar Cells

Spiro-MeOTAD is the most common HTM used in PSCs, and it employs the use of bis(trifluoromethane)sulphonamide lithium salt (LiTFS) and 4-tert-butylpyridine (TBP). To increase the HTM polarity and improve the interfacial electrode, TBP is employed. Li-TFSI is also added to enhance oxidation of the spiro-OMeTAD thus enhancing the conductivity and increasing the hole mobility. Buffer solutions are also introduced to overcome the negative effects of oxidation and corrosion and maintain long-term stability. PbI_2 can be dissolved by TBP solution according to the Rxn 2.2 to 2.4 (Ren *et al*., 2022).

$\mathrm{MAPbI_3} \rightleftharpoons \mathrm{MAI(s)} + \mathrm{PbI_2(s)}$ Rxn 2.2

$\mathrm{Pb_2\ (s)} + x\mathrm{TBP\ (s)} \rightarrow [\mathrm{Pb_2} \cdot x\mathrm{TBP}]\ \mathrm{(s)}$ Rxn 2.3

$\mathrm{Pb_2\ (s)} + x\mathrm{TBP\ (s)} \rightarrow \mathrm{Pb_2\ (s)} - \mathrm{TBP}x\ \mathrm{(aq)}$ Rxn 2.4

Thus, $MAPbI_3$ degradation leads to the formation of two solids in equation 2.1 above, which are PbI_2 and MAI(s). Progressively, a complex reaction is observed when PbI_2 reacts with TBP hence promoting the degrading of perovskite. HTM is thus used to protect the perovskite layer from corrosion and henceforth increasing the device lifetime (Ren *et al*., 2022).

Additionally, to solve the problem of instability, the PSC architecture has evolved over some time and the interfacial layers have been introduced for improved performance. This evolution has a major influence on the HTMs. The emergence of PSCs was to replace the dye/electrolyte used in DSSCs and for this reason, PSCs provide a varied range of the architecture as opposed to the other PV technology (Fakharuddin *et al.,* 2017). HTM-free PSCs have also been developed employing conducting interfacial engineering and optimizing the length of PSCs and transporting layers. (Fakharuddin *et al*., 2017).

2.4 Fabrication Techniques Employed

2.4.1 Spin Coating Fabrication Technique

Spin coating is one of the most cost effective and simple solution-processed method of uniform perovskite layers deposition method (Kajal *et al*., 2018). It is used to produce small-area solar cells. This method has produced a good efficiency over time of around 25.83% as compared to other fabrication techniques. This comparison is illustrated in Figure 2.4. The quality of the PSC produced by this method is optimized by setting spin time, speed and acceleration during spin coating. Very good reproducibility and morphology is achieved using this method. (Kajal *et al*., 2018). Although high quality perovskite active layer can be achieved by other methods such as blow drying, the other layers (HTL and ETL) are still spin coated to prevent hole blockage thus making the layer dysfunctional (Zheng *et al*., 2017).

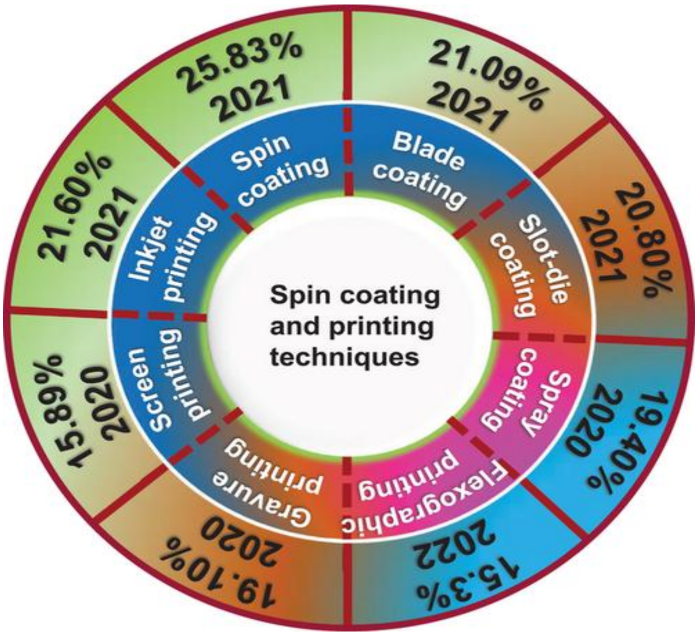

Figure 2.4: An overview of the highest PCE of PSCs using spin-coating and different printing techniques
Source: Parida *et al*. (2022)

2.4.2 Blade-coating

This printing technique can also be referred to as bar coating or knife coating. It is an important technique that applies the low-cost materials use to give wide-area coating and applies to both flexible and rigid substrates (Yang *et al*., 2022). On the substrate, ink is deposited and spread by the knife coater resulting to a thin wet film. The solution meniscus thus determines the thickness of the formed film and can also be managed by the blade's gap, the ink's viscosity, and the substrate's wettability. The blade's speed as well as the blade's geometry (Howard *et al*., 2019).

This technique has been extensively used and most frequently, it is confused with the single-step deposition method (Howard *et al*., 2019). However, their difference lies in the perovskite film crystallization where blade-coating, poses a lot of challenges than single-blade coating since the solvent evaporation is slower in blade coating as compared to single-step deposition. (Li *et al*., 2018; Jeong *et al.,* 2019). The perovskite film brought about by blade coating shows better optoelectrical properties with a higher efficiency of 19.23% (Parida *et al*., 2022). These results resulted from nucleation and larger-sized perovskite crystals enabling the perovskite solute to travel to the contact line (Parida *et al*., 2022). This method has been successfully used in the printing of ETL in fullerenes, TiO_2, ZnO, and SnO_2 as well as in HTL like PTAA polymers, PEDOT: PSS as well as small particles such as spiro-OMeTAD (Kim *et al*., 2015). Lee *et al.* (2022) have been able to come up with a better donor-acceptor-donor HTL 4-dicynomethylene-4H-cyclopental [2,1-b,3,4-b) dithiophene together with bis (alkoxy) diphenylaminocarbazol groups and PSCs printed through blade-coating on thermal assistance and an improved PCE of 21.09% resulted (Lee *et al.,* 2022).

Despite the success of the blade-coating method, it faced some challenges. These include: During blade coating at low solvents temperatures, intermediate solvates are formed leading to trap formation and poor surfaces. Beautifully, this problem was overcome by Li *et al.* (2018) cited by Parida *et al.* (2022) developed a higher performer transition control which is blade-coated by direct phase change to perovskite nucleus from sol-gel (Li *et al*., 2018). The blade-coated PSCs are in shapes like cylindrical bars (Jeong *et al*., 2019; Parida *et al*., 2022).

2.5 X-ray Diffraction (XRD) Machine

Materials such as minerals are arrangement of atoms forming a crystal microstructure. Using physical properties such as colour, hardness and crystallinity, materials can be characterised. X-ray diffraction is widely used for structural characterization of materials. When X-rays penetrate a material, the rays are scattered surrounding atoms nucleus. The scattered rays interferes with each other as they are emitted in different directions under constructive interference (Ali *et al*., 2022).

2.5.1 X-ray Diffraction Principle

X-rays are scattered when they impinge solid materials. The wave scattered are emitted in different directions and they undergo either constructively or destructively. There exists a closer correlation between diffraction and periodicity. Higher diffraction is seen at shorter periodicity. The XRD graphs for amorphous and crystalline solids are shown in Figure 2.5.

For amorphous material, XRD graph only indicate the maximum average peak for specific diffraction angle as opposed to a crystalline material with several distinct peaks. This is owing to the periodic arrangement for the atoms for crystalline material as opposed to the absence of periodic arrangement of amorphous material (Ali *et al*., 2022; Lamas *et al*., 2017). Information about atomic position and atomic number of the cell is illustrated by intensity of diffraction peak and on the other hand, information about the shape and size of a unit cell are provided by diffraction peak position (Ali *et al*., 2022; Lee, 2017).

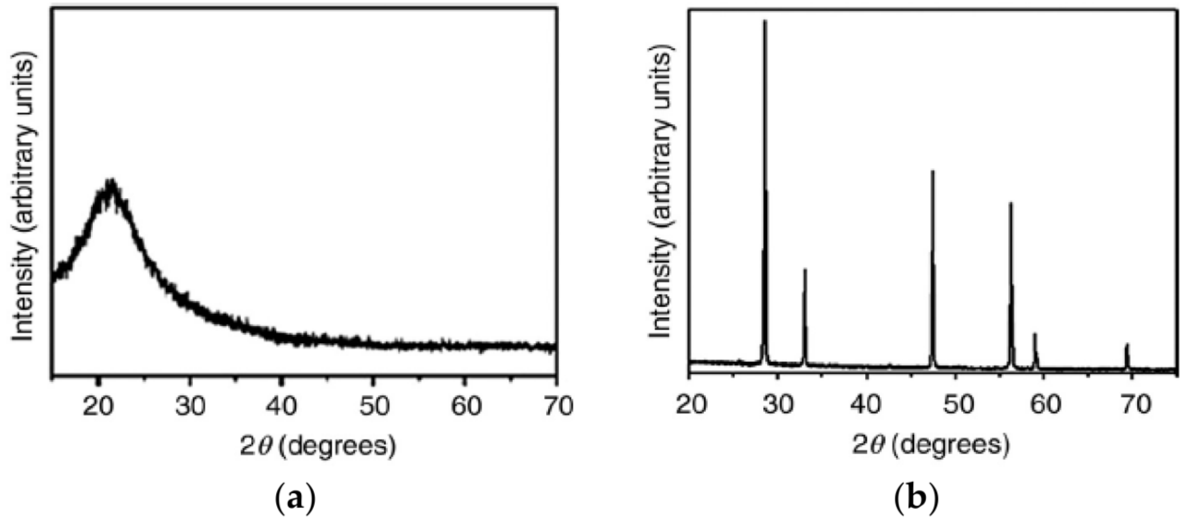

Figure 2.5: XRD qualitative plots for scattering intensities against scattering angles for a) an amorphous substance b) a crystalline substance
Source: Lamas *et al*. (2017)

The science behind diffraction is best explained by Braggs Law which is a special case of Laue diffraction, which determines the angles of coherent and incoherent scattering from a crystal lattice (Marcos, 2022). When X-rays are irradiated on a specific atom, they form an electronic cloud move looking like an electromagnetic wave. This charge movement radiates waves with similar frequency, slightly unclear due to different effects. This phenomenon is called as Rayleigh scattering. Generally, this principle elucidates the relationship between an x-ray light shooting and its reflection from surface of a crystal (Nath *et al*, 2020).

Bragg’s law conditions that when the X-ray is incident on a surface of a crystal, its incidence angle, θ, reflects the same scattering angle, θ. And, when the path difference, d is equal to a whole number, n, of wavelength, λ, constructive interference will occur (Marcos *et al.*, 2022). The particular process that occur after scattering neutron waves by nuclei or a comprehensible spin interaction with a secluded electron. These wave fields which are re-emitted obstruct with each other either constructively or destructively, creating a pattern of diffraction on detector. The diffraction analysis points to the resulting wave interference, and this investigation is known as Bragg diffraction. The Bragg’s diffraction is illustrated in Figure 2.6.

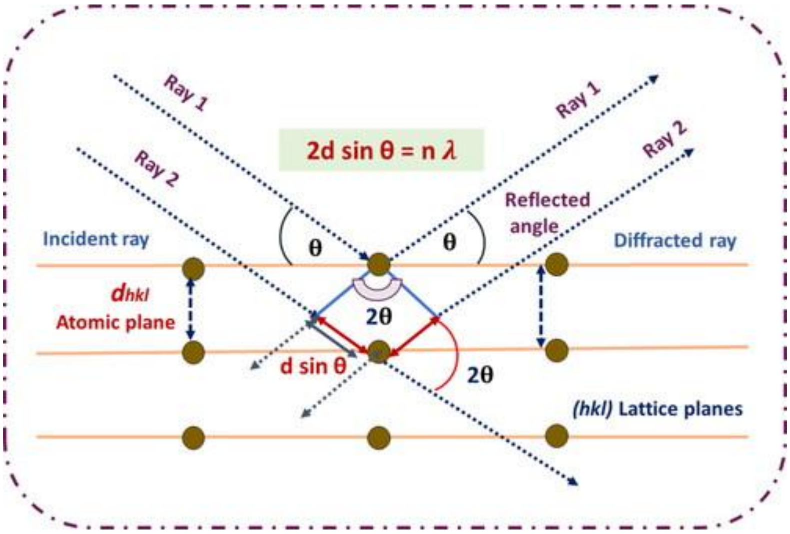

Figure 2.6: Bragg's law diagram

Source: Ukkunda *et al*. (2024)

$$n\lambda = 2d\sin\theta \qquad (2.1)$$

Where n is the order of diffraction

d is plane interval.

The energy E, of the corresponding quanta of X-ray can be obtained from the wavelength.

$$E = hf = \frac{hc}{\lambda} \qquad (2.2)$$

Where h is the planks constant (6.625x10^{-34} Js)

c is the speed of light (c=2.998x10^{8} m/s).

The relationship of energy and first order of diffraction is given by:

$$E = \frac{hc}{2d\sin\theta} \qquad (2.3)$$

According to the first equation (1); Bragg's Law, it clarifies why X-rays are reflected by crystals faces at certain angles of incidence (θ, λ). Similarly, *d* point to the distance between the layers of atoms, and λ the wavelength of the incident X-ray beam and n as an integer (Zhong *et al*, 2019)

2.6 Ultraviolet-visible Spectroscopy

The ultraviolet-visible (UV-Vis) spectroscopy method applies visible, ultraviolet and near infrared light ranges to determine its absorbance and transmittance by applying the Beer-Lambert law. The law relates light absorption to the sample properties through which the light is travels (Akash *et al*., 2020).The Beer-Lambert law states that:

$$A = \varepsilon Lc \qquad (2.4)$$

Where A is the absorbance, ε is the molar absorption coefficient (l mol^{-1}cm-1), c is the concentration (mol l-1) and L is the path length (cm). This shows linearity of absorbance in relation to concentration for low concentrations. From this, it can be shown that Beer-Lambert's law in simple terms states that the absorbance is inversely proportional to the transmittance of the solution under analysis (Akash *et al*., 2020).

$$A = \text{Log}\left(\frac{1}{T}\right) \qquad (2.5)$$

Where A is absorbance and T is transmittance

Absorbance occurs when light has reached a certain level in a material and the remaining will be transmitted or reflected depending on the material (Penner, 2017). Every amount of light is characterized with a specific amount of energy given by the formula below.

$$E = hf \qquad (2.6)$$

Where h is the planks constant and f is the light frequency. Since light has energy, it's able to excite electron from ground stable state to a higher energy state, resulting to absorbance at wavelength different for every molecule or samples. Larger energy gap between the energy levels requires wavelengths of higher energy, leading in absorption of shorter wavelength light (Penner, 2017). In this research work, UV-Vis spectroscopy was used to obtain band gap as well as optical properties such as absorption coefficient, reflectance and transmittance.

2.7 Progress in Lead-Based Perovskite Solar Cells

Asare *et al.* (2021) fabricated a hybrid HTL using PEDOT: PSS and copper-doped nickel oxide (Cu: NiO$_x$). Simulating finite elements using Abaqus/CAe determined the device's mechanical performance. The result indicated that when Cu: NiO$_x$ is included in PSC devices, it improves J-V behaviour, thus improving PCE from 11.5% and 9.8% obtained on using Cu: NiOx alone and PEDOT: PSS is doped alone to 12.8% obtained when PEDOT: PSS is doped with Cu: NiOx. This resulted from the improved electrical conductivity because of the provision of extra charges by Cu: NiOx to the absorber layer (Asare *et al.*, 2021).

Similarly, it was observed that degradation of PEDOT: PSS doped with Cu: NiO$_x$ was slower in comparison with HTL made of PEDOT: PSS, only which is attributed to its hygroscopic and acidic phenomenon which typically decays the photoactive layer (FTO) (Asare *et al* (2021). To achieve this, Asare *et al.* (2021) treated FTO for 15 minutes using UV-ozone. They prepared Cu: NiOx of 0.1 M to 0.2 M from copper (II) acetate monohydrate, nickel (II) acetate tetrahydrate, as well as 2-methoxy ethanol and put on FTO substrate for 30 s, followed by annealing at 400 °C air for developing Cu: NiOx nanocrystal structures for 30min.

After adding filtered PEDOT: PSS mixture at 4000 rpm for 60 s, the many-layered structure was then annealed at 130 °C temperature for 15 min, and perovskite solution was then prepared from 5% surplus lead perovskite precursor in the ratio of 1:3 of $Pb(OAc)_2.3H_2O$ lead acetate trihydrate to MAI. Spin coating of perovskite solution was done for 12 min at 80 °C leading to the formation of crystals of $CH_3NH_3PbI_3$ following the procedures outlined in Figure 2.7 (Asare *et al.*, 2021; Zhang *et al.*, 2015)

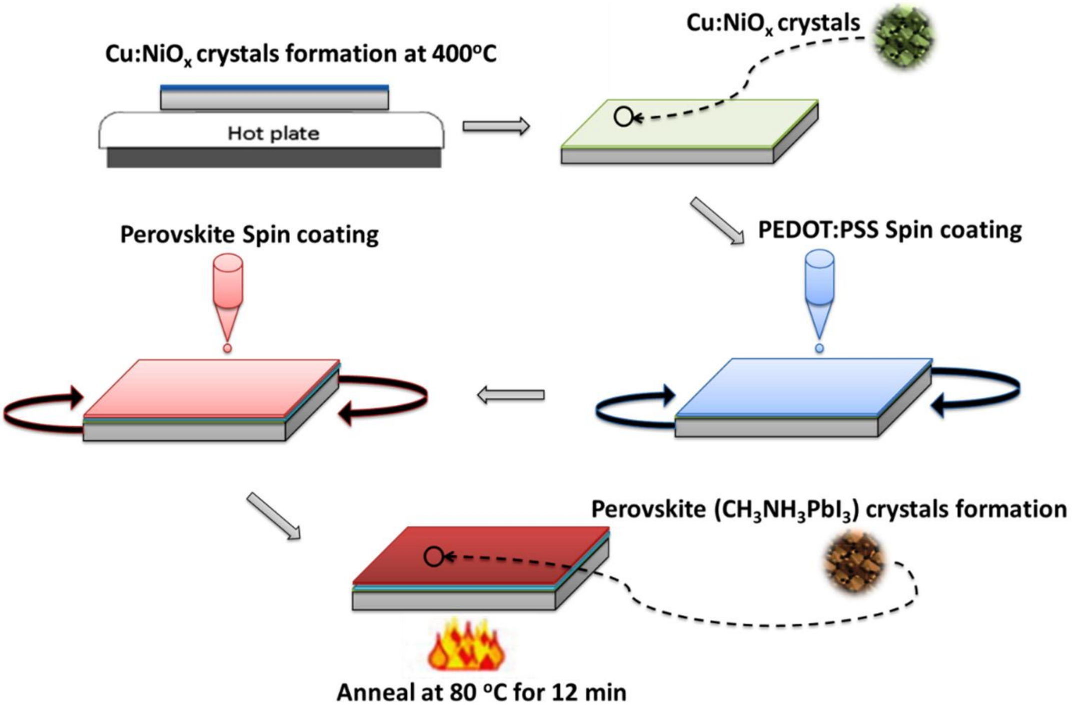

Figure 2.7: Schematic illustrating steps in Cu: NiO_x and perovskite Crystallisation
Source: Asare *et al.* (2021)

After deposition of 0.02g of PCBM of a litre of chlorobenzene solution and then sequentially on the $CH_3NH_3PbI_3$ /PEDOT: PSS/Cu: NiO_x/FTO substrates for the 60 s at 2000 rpm, the device obtained undergo difficult test such as scanning electron microscope (SEM) analysis, UV-vis spectroscopy, copy etc. The SEM test indicated that the Cu did not alter the microstructure: NiO_x/PEDOT: PSS composite, and the perovskite crystallization level was maintained, as shown in Figure 2.8. Moreover, the x-ray diffraction indicated similar characteristics of PEDOT: PSS only with FTO coating with PEDOT: PSS/Cu: NiO_x. Additionally, the UV-Vis optical characterization indicated that absorbance was majorly in the visible range with transmittance exceeding 80 %, which is similar to PEDOT and PSS alone (Zhang *et al.*, 2015).

Dual engineering applied on α-Phase $FAPbI_3$ Perovskite has comparatively high thermal stability, high PCE, and a narrow band gap and is thus preferred. (Zhang *et al*., 2019). To further enhance the performance and overcome phase transition to the unwanted $FAPbI_3$ hexagonal structure at average room temperature, which is optimum during high humidity, methylene diammonium dichromate ($MDACL_2$) is added. Hence, α-Phase $FAPbI_3$ is stabilised. This achieved PCE of 23.7% (Kareem *et al*., 2022; Zhang *et al*., 2019).

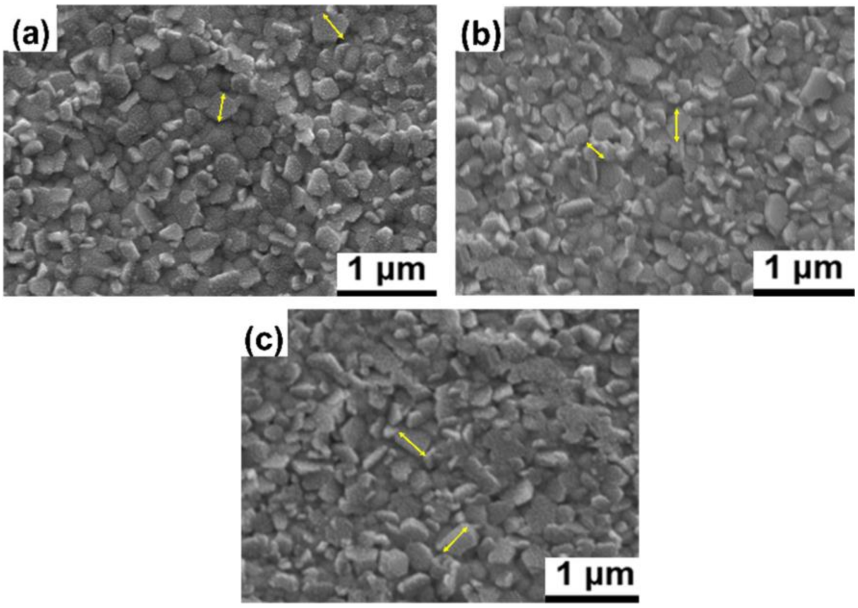

Figure 2.8: SEM images (**a**) perovskite/PEDOT: PSS/FTO/glass, (**b**) perovskite/PEDOT: PSS/0.1M Cu: NiOx/FTO/glass, (**c**) perovskite/PEDOT: PSS/0.2 M Cu: NiOx/FTO/glass Source: Asare *et al*. (2021)

Kareem *et al.* (2022) employed dimensional and additive modifications by inserting propionic into FAPbI3 to enhance $FAPbI_3$ film crystallisation, thus balancing the anion cation ratio. 2-(4-fluorophenyl) ethyl ammonium iodide (FPEAI) containing a p-type $NOBF_4$ was employed in 2D/3D heterostructure fabrication of high stability $NOBF_4$, gave out accelerated processes of charge transport in the perovskite/HTL interface and thus exhibiting a 23.17% PCE.

Lin *et al.* (2021) researched perovskite solar cells with embedded homojunction. The group showed that MHP polycrystalline film with departs of extrinsic ions of metal has a longer lifetime of around 5 μs when investigated with time-resolved microwave conductance (TRMC) as opposed to tens of nanoseconds passivated ions. This was achieved by adding Sr^{2+}, Ce^{2+}, and Ag^{+} to the polycrystalline MHP and studied effect on the solar cell performance. It was observed that the addition of the ions reduced decay time as opposed to ions of Rb^{+}, K^{+}, and

Na^+, and the PCE for MHP solar cells improved unexpectedly from 17.4 % to 18.4 %-19.4 % after the constituents were optimised (Lin *et al*., 2021). Moreover, adding these ions improved and stabilised the PCEs of FA0.85MA0.15 Pb (I0.85 Br0.15)$_3$ solar devices to 20.8 % from 18.7 %, and the photocurrent curves indicated ignorable hysteresis (Lin *et al.*, 2021).

Jeong *et al.* (2021) applied pseudo-halide engineering for PSCs involving α-$FAPbI_3$. Formamidinium iodide was synthesised by mixing 50 ml of hydroiodic and 25 g formamidine acetate in a flask of 500 ml followed by continuous stirring. After evaporating the solvent, a light yellow powder was obtained at 80°C, which was then added to ethanol for dissolution and precipitated in diethyl ether. After repeating the method thrice and obtaining white powder crystallised from the solvents in the refrigerator, the powder was collected and heated for 24 hours at 60 °C. 0.8 M FAI and PbI_2 were mixed in a 1:1 mole ratio in 2-methoxy ethanol of 22 ml. The solution was then stirred at 120 °C and applied the retrograde method for recrystallization, filtered the powder in a glass filter for 30 minutes at 150 °C for the synthesis of a black $FAbI_3$ and formamidine formate (FAHCOO, into excess formic acid, using rotary evaporation technique. The wet powder was recrystallized with ethanol, forming a plat-like crystal. Perovskite samples were obtained finally by grinding PbI_2 and FAI with FAHCOO of FABr in Retch bull Mill (MM-200) at 25 Hz for 30 minutes, then annealed for 15 minutes at 150 °C (Joeng *et al.*, 2021).

The group prepared an FTO glass substrate and cleaned using RCA-2 (H_2O_2-HCL-H_2O) to remove metal ion impurities and proceeded with ethanol, acetone, and isopropyl alcohol (IPA) cleaning for 15 minutes in an ultrasonic system—the applied spray-pyrolysis technique to deposit. TiO_2 (C-$TiOO_2$) compact layer, and then the substrate was stored for one hour at 450 °C and cooled. The Mesoporous TiO_2 layer was placed on top of the c-TiO_2 layer through spin coating TiO_2. The prepared FTO/e-TiO_2 substrates were then heated for 1 hour on a hot plate of 500°C and then cooled to 200 °C to remove organic compounds (Jeong *et al.*, 2021).

The perovskite layer was fabricated at room temperature and 20 % relative humidity with a perovskite precursor prepared by mixing 35 % MACL inside DMSO and DMF (4:1) and 1.139 kg FApbI3. Extra FAHCOO was included for the Fo-FAPbI3 film. The group dripped dimethyl ether of 1 ml after 10 s spinning during spin coating, and then the movie of the perovskite layer dried for 10 min in a 150 °C hot plate. Then, the IPA on the perovskite film was spin-coated. Spiro-OMETAD was deposited by spin-coating HTL at 4000 rpm for 30 seconds. Moreover, thermal evaporation deposited the electrode (gold) on Spiro-OMETAD.

On characterising the solar cell, a certified PCE of 25.2 % was obtained, with stability of more than 450 hours and more than 10 % strong electroluminescence (Joeng *et al.*, 2021).

Wang *et al.* (2019) obtained thermodynamically stabilised PSCs based on β-CsPbI3 with efficiencies of greater than 18 %. The group spin-coated a stoichiometric mixture of precursor solution of PbI_2.xDMAI where x= 1.2 or 1.1 into a TiO_2 compact layer. The organic species were identified and characterized using nuclear magnetic resonance, supported by XRD data, then evaluated the perovskite film composition and determined that it was utterly inorganic. The PSCs planer was fabricated with FTO and C-TiO_2. The best PCE of CsPbI was obtained as 15.1 % with a TSC of 20.03 $mAcm^{-2}$ (Wang *et al.*, 2019).

To further enhance the PCE, CHI was used in the spin coating, which improved the alignment of energy level by 120 MeV. Ultraviolet spectroscopy demonstrated a negligible absorption effect, and the XRD partners were almost identical. It improved to 15.2 %, but when β-CsPbI3 was used, the certified PSE obtained was 18.4 % (Wang *et al.*, 2019).

Zhong *et al.* (2020) investigated PCBM's role in PSC hysteresis suppression. The group dissolved PbI_2, CH_3NH_3I, and CH_3NH_3PbI-xCIx solution in a dry powder of dimethylformamide in a stoichiometric ratio of 3:1. Spiro-OMETAD was prepared and used fluorine-doped tin oxide the patterned it by the powder of zinc with HCL solution. FTO glasses were cleaned with acetone and 2 % hellmanex mixed with deionised water and isopropanol (Zhong *et al.*, 2020).

The group sprayed a compact TiO_2 layer with titanium diisopropoxide bis(acetylacetonate) in ethanol at 450 °C for 1.5 hours at ambient temperature. Electronic optimisation was done for PPCBM and PCBM thickness, followed by spin-coating PCBM in chlorobenzene for 30 seconds at 3000 rpm and then annealing at 100 °C. PCBM layer was also spin-coated by $CH_3NH_3PbI_{3-x}Cl_x$ perovskite solution for 20 seconds at 3000 rpm. As spun films, annealing was conducted after nitrogen clove box drying for 1.025 hours at 105 °C (Zhong *et al.*, 2020).

The spiro-OMETAD HTL solution was spin-coated for 3 seconds at 4500 rpm; they were fabricated in a nitrogen-filled area (Zhong *et al.*, 2020) and transported at night for oxidation of spiro-OMETAD. Perovskite film was then prepared for PL imaging microscopy. Using the Keithley 2400 source meter, J-V device measurement was done at a scanning speed of 0.8 V as scanning speed with a 0.2 V to 0.1 V voltage range. The powder circle number was 0.1. The ions of the iodine were observed on migration using wide-field photoluminescence imaging. PPCBM does not suppress this migration, but PCBM efficiently suppresses them.

The reduction of energy actuation in PCBM and XRD photoemission results demonstrated that temperature depends on chronoamperometric results.

Zhu *et al.* (2020) designed amphiphilic molecule mitigators to improve stability and achieve a PCE of 23.5 % using agent-based enbenzylammonium iodide. 4-tert-butyl-benzylammonium iodide (tBBAI) was synthesised. XRD revealed that the butyl/substitution group disallows unrequired aggregation by steric repulsion. The increased photoluminescence revealed an outstanding passivation ability followed by Quasi-Fermi splitting (ΔE_f) of the perovskite films, thus leading to a high open circuit voltage (Voc) of 1.142 V. The perovskite used iodine rich of 97:3 for I to bromine with a 1.55 eV band gap. The device indicated 410 mV optimised voltage loss of approximately a radiative limit of 90 %. Which is among the minor voltage losses of the PSCs in time-resolved photoluminescence; it is revealed that there is an enhanced transfer of charge with the interfacial layer of tBBAI to the HTL from the absorber layer as opposed to the control devices and associated to the hole-extraction beamer owing to improved contact between non-polarised HTL and polarised absorber layer leading to an improved fill factor of 82 % from 75 % there is better moisture resisting. Result in a combined PSCS of 23.5 % of this mesoscopic PSCs and FF and Voc of 82.1 % and 1.142, respectively, the PV performance of 95 % is retained by tBBAI passivated PSCs with an operation period of 500hours under simulated full-sun irradiation (Zhu *et al*., 2020).

X-ray photoelectron spectroscopy (XPS) was used to characterise surface elemental properties for passivated perovskite. The XRD spectrum revealed that no additional diffraction peaks suggest an amorphous morphology for the passivation layer owing to increased steric hindrance because of the substitution of tert-butyl in tBBAI. TPRL was measured to demonstrate the photoelectronic properties of the passivated perovskite films (Zhu *et al*., 2020). PL rapid decay was attributed to carrier diffusion prompting carrier concentration fast decay on the front surface presence of midgap trap, which is positively charged in halide perovskite which, once filled, becomes neutral, l thus exhibiting low capture cross-section for holes and HTL hole injection leading to rapid PL signal decay. The PEAI-treated film indicates HTL hole extraction, which is faster than untreated. A smaller hole transfer beamer probably triggers it, and it is outstanding in tBBAI, which outperforms it completely. Thus, tBBAI exhibits less charge recombination and is more stable (Zhu *et al*., 2020).

Duan *et al*. (2024) achieved efficiency of 21.41 % using $CsPbI_3$ by effective redox method with 4-fluorobenzothiohydrazide in the precursor solution. It was attained by preparing TiO_2 layers on FTO by chemical bath deposition method. This was followed by injection of ultrapure water and titanium dioxide then put into electric blast drying at 70 °C for 55 min. The deposited TiO_2 was then annealed for 30 min at 200 °C and treated for 55 min with ozone. The $CsPbI_3$ precursors were then spin coated into FTO for 10s at 1000 rpm and 3000 rpm for 40 s. This was followed by spin coating of Spiro-OMETAD at 5000 rpm for 30 s then gold electrode deposition (Duan *et al*., 2024).

2.8 Lead-Free Perovskite Solar Cell

Despite lead halide showing a very high PCE of above 20 % (Yang *et al*., 2017), due to its toxicity, more advancement has been introduced to substitute lead with other metals such as tin, antimony, and bismuth as well as using halide double perovskite. To begin with, tin shows promising properties as it continually shows a rising PCE above 13 %. It is the most appropriate since it lies in the same group as lead, thus indicating desirable similarities, as demonstrated in Figure 2.9 (Chakkamalayath *et al*., 2022; Yang *et al*., 2021).

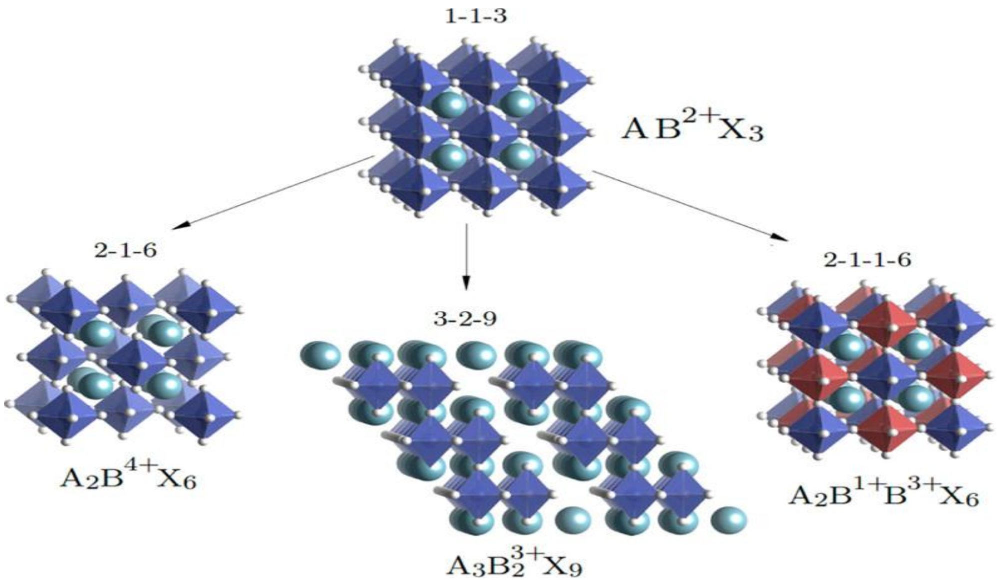

Figure 2.9: Schematic comparison between lead-free perovskite and lead perovskites and lead perovskite structures
Source: Giustino and Snaith (2016)

The hot injection technique and vapour-supported processing of solution are applied in preparing $CH_3NH_3SnX_3$ (x can be Br, Cl, and I) films of perovskite solar cells. Excess SnX_2 develops a phase, hence improving the stability of the air. The optoelectronic properties of PSCs of mixed tin halide have indicated anomalous features with a change in concentration of $SnCl_2$ leading to a shift in the band gap, i.e., the more the concentration, the larger the band gap. Caesium tin halide provides an alternative route. Although antimony (Sb) and bismuth

(Rb) are similarly suitable substitutes for lead, their PCEs are slightly lower than tin. For example, sulphur-doped bismuth halide shows a good band gap ideal for PSCs (Yang *et al.*, 2020). Moreover, halide double perovskites as lead substitutes are attracting much interest since they indicate double metal ions for obtaining the required structure (Cai *et al.*, 2020). A combination of Ag^+ and Bi^{3+} is necessary to occupy two sites in 3D PSC architecture, forming a double perovskite, as indicated in Figure.2.10.

Nishimura *et al.* (2020) fabricated halide PSCs by lead-free tin using FTO/PEDOT: PSS (Gelz doped Sn-perovskite/P3HT/Ag/Au through spin coating technique by cleaning it for 20 minutes with oxygen plasma and annealing it for 20 minutes at 150 °C. This is followed by 50 minutes of spin coating at 5000 rpm with an ant chlorobenzene solvent. The perovskite film was then annealed for 20 minutes on a plate of 70 °C, then added EDA diluted to 0.05m into perovskite film, resulting in a 0.405 cm active area. FTO/PEDOT: PSS (Gelz-doped Sn-perovskite/P_3HT/Ag/Au was fabricated for space charge limited current (SCLC) (Nishiruma *et al.*, 2020).

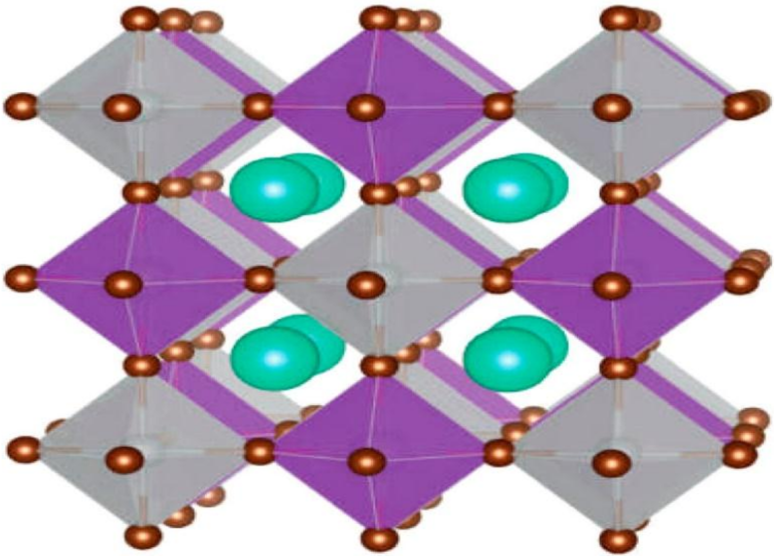

Figure 2.10: Halide double perovskite $Cs_2AgBiBr_6$ Cubic crystal structure. Brown-bromine, Light grey-silver atoms, turquoise-caesium, and purple–bismuth
Source: Savory *et al*. (2016)

JASCO V-670 UV-VS spectrophotometers was used for optical characterisation. A highest PCE was recorded when cations were mixed in the composition of GeI_2 doped ($FA_{0.98}$ $EDA_{0.01}$) $EDA_{0.01}$ SnI_3. They obtained 11.75 % PCE on using 0.7 V. Upon performing passivation, they achieved an improved efficiency of 13.24 %. The electron-rich group found

(=NOH) neutralised the oxidation of Sn^{4+} to Sn^{2+}, thus creating a high crystallinity film with superior dynamic charge properties and reduced density defect. A stable and highly efficient PCE was obtained. These lead-free PCEs achieved 11.2 %, which is a good improvement over the lead-free PCEs (Nishiruma *et al.*, 2020; Zhang *et al.*, 2022).

Wu *et al.* (2018) prepared a highly stable lead-free double perovskite Cs_2 $AgBiBr_3$ at 110 °C, allowing the solution to cool overnight at room temperature. They then fabricated it by cleaning indium tin oxide in acetone water and ethanol for 30 minutes, then retreated plasma oxygen for 10 minutes. Spin coating SnO_2 then made a layer of ETL in deionised water at 3000 rpm speed and annealed for 30 minutes at 150 °C. The double $CsAgBiBr_6$ was formed and dissolved in DMSO, then moved at low pressure and pumped to 20 Pa, proceeded by annealing for 10 min at a different temperature (Wu *et al.*, 2018), and the spin coating was further done for 30 seconds at 2000 rpm. XRD characterises the results by irradiating it with monochromatic light of λ=1.5418 A, and UV-V is used to investigate the absorption of visible light. Besides, high resolution was recorded by SEM. TRPL results were indicated by an ultra-first lifetime spectrometer and a Keithley source meter (2611), which illustrates the photovoltaic performance. A J-V scan of 0.13 Vs of 100 ms sweep delay was performed. The device achieved high stability without the high quality of the film and with a PCE of 1.44 %. Table 2.1 indicates Jsc, Voc, FF, and PCE at different annealing temperatures (Wu *et al.*, 2018).

Table 2.1: $Cs_2AgBiBr_6$ films performances at different annealing temperatures

Sample	J_{sc} **[mA cm^{-2}]**	V_{oc} **[V]**	**FF**	**PCE (maximum) [%]**
$Cs_2AgBiBr_6$ (150 °C)	0.76 ± 0.05	1.02 ± 0.01	0.63 ± 0.04	0.49 ± 0.05 (0.54)
$Cs_2AgBiBr_6$ (250 °C)	1.78 ± 0.03	1.07 ± 0.01	0.69 ± 0.03	1.32 ± 0.05 (1.37)
$Cs_2AgBiBr_6$ (300 °C)	1.79 ± 0.08	0.99 ± 0.02	0.65 ± 0.04	1.16 ± 0.06 (1.22)

Source: Wu *et al*. (2018)

Wu *et al.* (2018) applied the stoichiometric composition of $Cs_2AgBiBr_6$ for high-efficiency lead-free PSCs. In doing this, they prepared vacuum-processed $Cs_2AgBiBr_6$ films by synthesising $AgBr/BiBr_6/CsBr$ in the ratio of 1:1:2 in HBr through reflux, evaporation decanting, crystal growth as well as washing the $Cs2AgBiBr_6$ solution then dropping it on TiO_2 followed by spin-coating it in DMSO. They sublimated the compound and obtained it through sequential deposition of Cs_2Br, $BiBr_3$, and AgBr at a 5.0×10^{-4} Pa pressure, as shown in Figure 2.11.

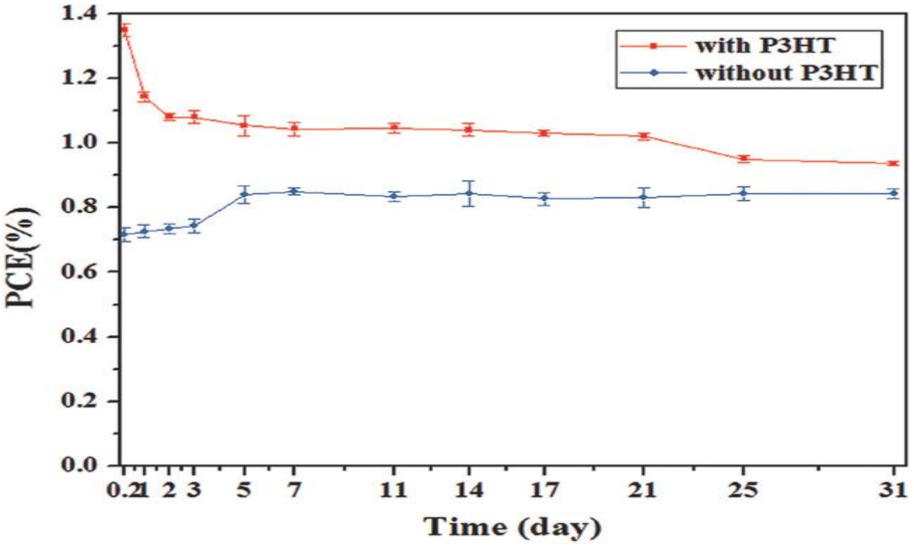

Figure 2.11: $Cs_2AgBiBr$ stability without encapsulation
Source: Wu *et al*. (2019)

$Cs_2AgBiBr_6$ was obtained by subsequent annealing at 280 °C after 220 °C. The morphological properties were investigated using XRD at the annealing temperature. The electronic structure of $Cs_2AgBiBr_6$ was determined through XPS analysis, which presented Cs 3d, Br 3d, and Ag 3d. The fabricated sample was tested for photovoltaic performance and obtained 2.51 % (Wu *et al*., 2018).

Gamal *et al*. (2021) used $Zn_{1-x}Mg_xO$ in simulation instead of TiO_2 as a buffer layer since it changes the band gap necessary for free electron conduction in ETL. As Mg concentration increases, the buffer layer energy gap increases, thus enabling the light from the sun to be transmitted in a range of UV light. Excellent performance was obtained when x=0.25 with PCE of 17.09 % and a band gap of 3.82 eV (Gamal *et al.*, 2021). This gave PCE of 21.66 % for the optimised device and 36.33 % at HTL, indicating 0.95 V open circuit voltage (Voc) with 33.85 mA/cm^2 as the short circuit current density (Jsc) and 82.01 % fill factor. Therefore, they concluded that lead-free $CH_3NH_3SnI_3$ PSCs indicate higher efficiency when using a more comprehensive band gap buffer layer. It is further influenced by optimisation thickness as well as solar cell layers doping, impacting significantly on the performance (Gamal *et al.*, 2021).

Tan *et al.* (2020) synthesised double perovskite materials by applying the hydrothermal technique. An autoclave Teflon with high-purity raw materials and aquaria WAS SOAKED, followed by the dissolution of 2 moles (CsC) in 5 ml of HCL of 10 M in a Teflon autoclave of 25 ml. They then added one mmol of $SnCl_4.5H_2O$ and x-mmol of $TeCl_4$. The solution was heated for 12 hours at 180 °C in a stainless pan autoclave, followed by steady cooling of 5 °C per hour to 30 °C. The crystals synthesised were then filtered, cleaned with acetone, ethanol, and acetonitrile, and then furnace-dried overnight at 60 °C (Tan *et al*., 2020).

The $Cs2Sn_{1-x}Te_xCl_6$ obtained was characterised by X-ray diffraction after grinding its crystals to powder using a PANalytical Xpert PRO diffraction meter called Cu-Kαradiation with graphite micrometre on the reflection mode. Using the FULLPROF package Rietveld refinements were conducted, and the UV-VS (Perkin Elmer instrument, Lamda 950) were used to record the absorption spectra, and then, using reference material were calibrated consecutively. Hariba Jobin Yvon Raman Spectrometer was applied by Tan *et al*. (2020) for measuring photo luminescence, which is dependent on temperature in the range of 80 K to 323 K (Tan *et al*., 2020).

They calculated density function theory using the projector augmented wave in VASP code after something cut off energy as 350.0 eV and 243 atoms super cell (Saidi *et al*., 2012). The Brillouin zone used is Γ-only K-mesh. They also applied par dew- Burke-Emzerhf (FBE) and generalised gradient approximation (GGA) functional in calculating the total energy and structural relaxation, n and each atom was at 0.01 eVA^{-1}. Heydscuseni ernzerhef (HSE) functional was applied in electronic characterisation to predict a band gap than GGA-PBE better. The results indicated a 95.4 % quantum yield of photoluminescence and good anti-water stability, which can be used in double halide PbCs (Tan *et al*., 2020).

Hu *et al.* (2023) fabricated and characterised inverted 4-T perovskite tandem solar cells. Solar cells use antimony potassium tartrate to stabilise the wide-band gap. They used patterned ITO, which they cleaned ultrasonically in deionised water with detergent, acetone, and ethanol for 15 minutes and blew with nitrogen to dry. They treated it for 15 minutes with ozone, transferring the sample into an N_2-filled glass glove box. The group then spin-coated it at 3000 rpm for 30 s, annealed it for 10 minutes at 100 °C then mixed CsI, PbI_2, FAI, $PbBr_2$ in a mixture of DMF and DMSO in a ratio of 3:1 of 1.4 M (Hu *et al*., 2023).

They then added antimony potassium tartrate to 1ml precursor, and the solution was deposited onto the MeO-$2PAC_2$ layer. Diethyl ether was added, and thermal annealing was performed for 5 minutes at 100 °C. A buffer layer of SnO_2 was deposited at 90 °C using tetrakis and pure water as precursors. This was a wide band gap perovskite solar cell. The SEM characterisation illustrated that the cross-sectional morphology assisted the perovskite better and gave a PCE of 20.35 %. On preparing a 4T tandem solar cell, a PCE of 26.3 % was found (Hu *et al*., 2023).

In attempt to suppress the charge recombination in tandem devices with front side flat Si-wafers, Turkey *et al*., (2024) used phosphoric acid called 2, 3, 4, 5-pentafluorobenzyl in perovskite ink near perovskite/C_{60} interface and SiO_2 nanoparticles and thus enhancing the number of pinholes and shunts brought about by pFBFA at the same time allowing use of Me 4PACs for hole transport layer. After bringing these together; the device was electrically and optically optimized giving a PCE of 30 % and certified PCE of 30.9 %. In this experiment, pFBPA was applied to enhance the performance of top cell and as additive. SiO_2NPs was used to enhance the perovskite film quality and wettability. This was made of Phosphorus doped amorphous silicon layer, layer of silicon wafers, layer of zirconium doped indium oxide (IZrO) and silver contact electrodes deposited on ITO substrate (Turkey *et al*., 2024).

2.9 Stability Progress of Perovskite Solar Cells

Shi *et al.* (2020) applied gas chromatography-mass spectrometry to evaluate encapsulated stable PSCs. They determined whether solar cells could withstand the outdoor conditions by repeatedly exposing them to a -40 °C to 85 °C range temperature and a relative humidity of 85 %. They named the composition of the gas chromatography-mass spectroscopy (GC-MS) (Shi *et al*., 2020).

Using this technique, they separated the mixture components and determined the chemical structure of each component using spectrometry. They could directly specify the product of decomposition through many cation perovskite precursors filled cells at high temperatures. They thus identified thermal degradation routes by finding the heating temperatures from the out-gassing products (Shi *et al*., 2020). Sequentially, GC-MS was also used for packing techniques effectiveness evaluation for developed PSCs where the schemes were polyolefin blanket encapsulation, polyisobutylene (PIB) blanket encapsulation, and PIB edge seal where the layer of packaging glass cover capped, edge seal sample by a syringe for gases decomposing and using IEC photovoltaic module standard heat for testing feasibilities as well as using humidity freeze testing CH_3I, NH_3, and CH_3Br(MABr), $HC(NH_2)_2I$(FAI) and CH_3NH_3I(MAI) being the proposed and mixed halide $(MABr)_{0.15}$ + $FAI_{0.85}$ perovskite precursors (Shi *et al*., 2020).

GC-MS results confirmed the bromine-containing precursor. One-fifth of the gas was FAMA, and the remaining Cs were for CsFAMA. FAI undergoes reversible decomposition; however, when FA and MA are mixed, the product's decomposition undergoes an irreversible secondary reaction. They, therefore, conclude that GC-MS can identify products of organic perovskite decomposition under stress, thus illustrating the decomposition pathway. These are important for the potential cell stabilisation process since solar cells experience high operation temperatures in the field. It also confirmed pressure-tight encapsulation at a low cost, thus suppressing the outgassing of standard PSC photovoltaic modules (Shi *et al*., 2020).

Shi *et al.* (2020) obtained a 21 % thermally stable PSC of PCE. They introduced Lewis's base (biuret) as a perovskite precursor additive, which acted as a donor for coordination with lead iodide (PbI_2). This led to intermediate phase formation, which slowed down the crystallisation rate. The cross-linking biuret structure with the adjacent perovskite crystals was enhanced for excellent $MAPbI_3$ thermal durability. This leads to an increase in grain size and perovskite sizes and a decrease in density defects. The constants achieved for 12 days were 85 °C for $MAPbI_3$ with a PCE of 21 %. It is significant to know that they evaluated thermal stability under continuous thermal annealing in the presence of nitrogen at 85 °C. A stability positive effect was demonstrated by the introduction of biuret on the $MAPbI_3$ unsealed devices with a 94 % after 12 days of its initial frequency. The device stability was similarly evaluated in the 20-25 °C ambient temperature and 30-40 % relative humidity using the encapsulated cells in the dark and contrast; the preservation is 81 % for 1000 hours as opposed to 93 % for 1000 hours for biuret-modified devices which are, therefore, more stable in the natural environment. They ascribed the enhancement of air stability to improved morphology and crystallinity of perovskite-modified films by biuret and surface passivation of defects and the residual biuret given boundary (Shi *et al*., 2020).

Gao *et al.* (2019) added nanoparticles of $CsPbBr_3$ perovskite as an additive for stable perovskite, which are environmentally solar cells and achieved a PCE of 20.46 %. They used Cs_2CO_3 of 0.814 g, 25 ml oleic acid, and 30 ml octaclecene to synthesise a Cs-oleate solution. These were mixed in a 100 ml flask, and the solution was kept at 120 °C and protected by N_2 for 1 hour. The solution was heated to 150°C further and left to complete dissolution in $CsCO_3$ by maintaining for 3 hours. For $CsPbBr_3$ NP synthesis, ODE and $PbBr_2$ were transferred to a 50 ml 3-enclosed flask using a general hot injection technique (Gao *et al*., 2019).

XRD patterns of $CsPbBr_3$NPs show that it is indexed into cubic phase. Optical properties were investigated by measuring PL emission spectra and absorption of $CsPbBr_3$NPs. They reported that NPS controls the film growth of the perovskite, which approaches high crystallinity, fewer defects, and large grain sizes (Gao *et al*., 2019). The introduction of $CsPbBr_3$NPs improves the crystallisation quality of $MAPbI_3$ films. The passivation layers $Cs_{1-y}MAyPbI_3$-xBrx formed on $MAPbI_3$ lead to improved charge collection. The method was also seen as highly reproductive for 40 cells with a PCE of 20.10 % under AM 1.5 illumination. As illustrated above, the PCE achieved was 20.46 % with enhanced stability (Gao *et al*., 2019).

Mattaparthi *et al.* (2023) investigated Au/NiO/$FASnI_3$/$ZnO_{0.25}S_{0.75}$/FTO for economically friendly perovskite device structure using SCAP-1D where an absorber layer is zinc oxy-sulphide (ZnO:S), hole transport layer-nickel oxide (NiO) and absorber layer as $FASnI_3$. They varied the active layer $FASnI_3$ thickness, doping concentration, and defect density. The simulated device showed solar performance with a high FF of 89.64 %, a low short circuit current of 28.35 mA/cm^{2,} and a good open circuit voltage (Voc) of 1.2419 V. They obtained a higher PCE of 31.57 % for economically friendly and lead-free perovskite solar cells (Mattaparthi *et al*., 2023).

CHAPTER THREE

MATERIALS AND METHODS

3.1 Substrate Cleaning Procedure

ITO substrates were cleaned with hellmanex solution 2% in deionized water and then ultrasonicated in bath with Hellmanex solution for 15 minutes at 40 °C. This was followed with washing in with deionized water. Ultrasonication in bath with water for 15 minutes at 40 °C proceeded. Acetone was then used for rinsing the substrates followed by ultrasonication in acetone for 15 minutes at 40 °C. Rinsing with isopropanol followed. After the rinsing, it was ultrasonicated for 15 minutes at 40 °C in isopropanol. The substrates were then dried with nitrogen compressed gas for ozone treatment for 15 minutes. After ozone treatment for 15 minutes, FTO were then kept in the ozone for 30 min and then transferred in glove box for fabrication.

3.2 Synthesis of ZnO:S

The zinc acetate (ZA) ($Zn(CH_3COOH)_2$) and thiourea (TU) ($SC(NH_2)_2$) precursor materials were used. ZnO precursor was first prepared. This was achieved by dissolving 0.5M of ZA in deionized water and stirring in the magnetic stirrer. This was followed by Sulphur precursor preparation by dissolving 0.04M of thiourea in deionized water. The two precursor solutions were then mixed and ammonia solution added dropwise. This mixture was ultrasonicated and operated at a frequency of between 20 kHz and 750 Hz with power setting of 187.5 W. After 2.5 hours, the precipitates were collected and dried in an oven at 100 °C overnight. For other doping concentrations, the moles of thiourea were varied to 0.02M (4% sulphur doping) and 0.08M (16% sulphur doping) (Panda *et al*., 2013).

3.3 Synthesis of $FASnI_2Br$

1.2 nominal M tin (II) iodide (SnI_2) was prepared as a stock solution. 1 M of Ethylenediammonium diiodide ($EDAI_2$) stock solutions was similarly prepared. DMSO free solvents mixture of *N*,*N′*-Bis(3-pentyl)perylene-3,4,9,10-bis(dicarboximide) (DEF) and 1,3-Dimethyl-3,4,5,6-tetrahydro-2(1*H*)-pyrimidinone (DMPU) was prepared in the ratio of 6:1 volume to volume. These were prepared at a controlled temperature of around 22 °C. Right amount tin bromide ($SnBr_2$) and SnI_2 were weighed for making 1.2 M stock solution. DEF: DMPU was added to $SnBr_2$ and SnI_2 and left in a mechanical stirrer overnight at 650 rpm. $EDAI_2$ of 1 M nominal stock solution was also prepared in DEF: DMPU 6:1 v/v and kept overnight in a thermal shaker at 20 °C. The vials were wrapped with parafilm to prevent the lids from opening. The following day, $FASnI_3$, $FASnI_2Br$ were prepared. SnI_2 solution and with FAI solution were mixed while maintaining 1:1.1 mole ratios of FAI: SnI_2 for $FASnI_3$. The final solution was left in a mechanical stirrer overnight at a setting of 650 rpm at 20 °C. For $FASnI_2Br$, FABr and SnI_2 were mixed at 1:1.1 mole ratio. The resultant solution was left in a mechanical stirrer overnight at a setting of 650 rpm at 20 °C. All the vials were similarly wrapped with parafilm to avoid undesired unwind. For thin film formation, $FASnI_3$ and $FASnI_2Br$ were at 8:1 mole ratios and put in a mechanical stirrer at setting of 650 rpm and 20 °C temperature. 100 μL of perovskite material was spread on ITO substrate for perovskite film formation and then starting a spin coating program set in steps. 500 rpm for a duration of 5 s, 4000 rpm for 1 s, and 4000 rpm for 40 s. After 20 s from the start of the spin coating program, 100 μL of anhydrous diethyl ether was fastly deposited using a 1 cm tip cut pipette. The substrates were annealed on a hot plate for 30 min at 100 °C. The $FASnI_2Br$ perovskite film was obtained both on clean glass slide, on ZnO and on PEDOT-complex (HTL3 Heraeus) for checking how the film for n-i-p and p-i-n perovskite solar cells where ZnO represent the n-i-p and PEDOT-complex (HTL3 Heraeus) represent the p-i-n structures.

3.4 Characterization of $FASnI_2Br$ and ZnO:S

Structural characterization of the prepared samples of $FASnI_2Br$ and ZnO:S was done using X-ray diffraction (XRD) by applying Bragg's. Optoelectronic properties was also obtained by using ultra violet-visible light spectrophotometer (UV-Vis machine). These were done at BESSY II, Berlin Germany.

3.5 Fabrication of a Solar Device Using $FASnI_2Br$

100 µL PEDOT: PSS solution dissolved in anhydrous toluene at 1:4 volume ratio was spin coated at 500 rpm for 5 s then 4000 rpm for 40 s. Immediately, it was transferred onto hot plate at 150 °C for 10 min. 100 µL Al_2O_3 nanoparticles interlayer dispersed in IPA at 1:200 volume ratio was spin coated using same program (500 rpm for 5 s then 4000 rpm for 1 s and 4000 rpm for 40 s), transferred onto the hot plate at 100 °C for 5 min. 100 µL. $FASnI_2Br$ was spin coated using the same program (500 rpm for 5 s then 4000 rpm for 1 s and 4000 rpm for 40 s). At 21st second, 100 µL of anhydrous diethyl ether from 1 cm cut p1000 pipette was fastly deposited. Then transferred onto the hot plate at 100 °C for 30 min. C60/BCP/Ag are then thermally evaporated. C60 using 0.1–0.2 A/s rate for 50 nm, BCP at rate of 0.1 A/s for 7 nm and Ag at 0.1–1 A/s FOR 150 nm. The device is then kept overnight for J-V characteristics.

3.6 Fabrication of a Solar Device Using ZnO:S

Nickel (II) acetate tetra hydrate was dissolved in 2-methoxyethanol (for NiOx). 100 µL was spin coated 100 µL on a clean ITO glass substrate at 4000 rpm for 40 s. It was then annealed at 300 °C for 30 min. 1 mM Me-4pacZ was prepared in ethanol then spin coated at 5000 rpm for 30 s. $FAPbI_3$ solution was made by dissolving it in DMF: DMSO mixture. It was spin coated at 1000 rpm for 10 s then 5000 rpm for 30 s. ZnO:4%S suspension was made by dissolving 10mg/mL in isopropanol. This was spin coated at 4000 rpm for 30 s then annealed at 150 °C for 30 min. 10mg/mL of PCBM solution was made on chlorobenzene then spin coated at 2000 rpm for 30 s and then annealed at 100 °C for 5 min. 100 nm silver electrode was evaporated and then the device characterised for J-V characteristics. Box plots were also generated to determine best performing devices between ZnO:4%S and ZnO:8%S.

3.7 Device Characterization

This was done using solar cell I-V test system. The fabricated perovskite solar cell was illuminated under a solar simulator, and a current-voltage sweep is performed. From this, Voc and Jsc can be obtained. Both the fill factor and the efficiency are then calculated as below:

$$\eta = \frac{J_{SC} \text{ x } V_{OC} \text{ x } FF}{P_{in}} \tag{3.1}$$

$$FF = \frac{P_{max}}{J_{SC} \text{ x } V_{OC}}, \tag{3.2}$$

CHAPTER FOUR

RESULTS AND DISCUSSIONS

4.1 ZnO:S

The material was synthesized for electron transport layer, characterized and applied in perovskite solar device. The characterization results are shown below.

4.1.1 Structural Properties of ZnO:S

The X-ray patterns for sulphur doped ZnO at different doping concentrations is shown in Figure 4.1 below. It confirms the synthesis of the required material showing the formation of hexagonal wurtzite phase of ZnO with 100, 002, 101, 102, 110, 103, 200, 112, 201 patterns (Marković et al., 2019; Panda *et al*., 2013; Sterrer & Freund, 2014). New phases were seen (indicated by arrows). It can be seen that the peak length reduces with increase in doping concentrations.

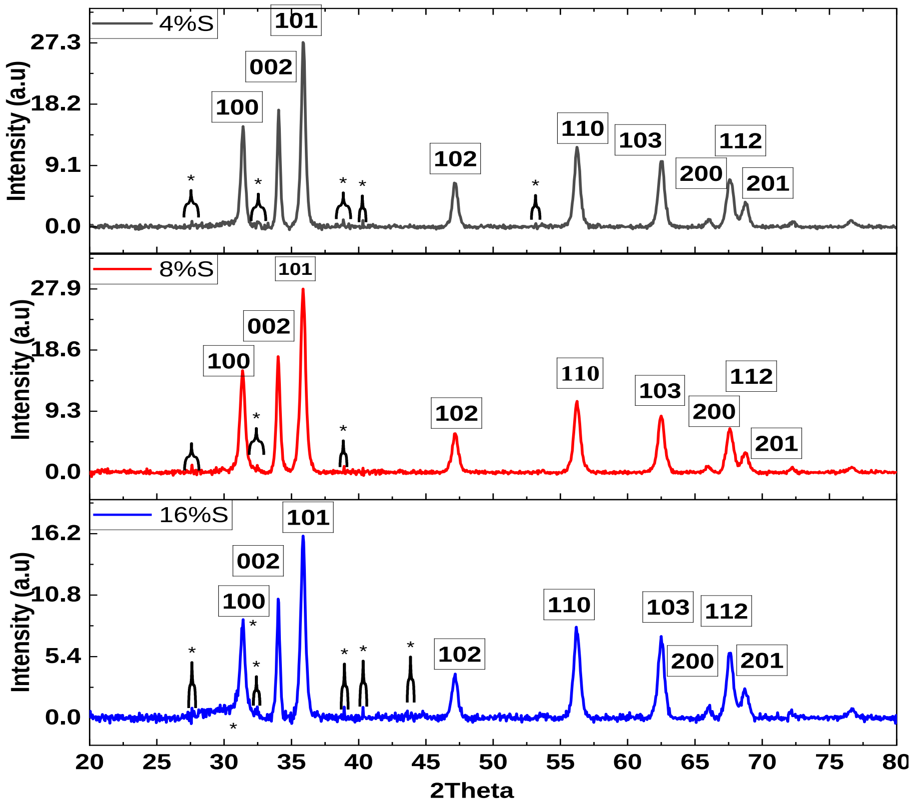

Figure 4.1: X-ray diffraction patterns for ZnO:4%S, ZnO:8%S and ZnO:16%S

4.1.2 Optoelectrical Properties of ZnO:S

Generally, from Figure 4.2, the transmittance of sulphur doped ZnO decreases with increase in sulphur concentration. This indicates that increase in sulphur concentration is more significant where the increased absorption is required. But where more transmittance is required, less doping is desirable. The transmittance also varied with wavelength across the visible and near-infrared region. At 4% doping concentration, the result shows highest transmittance across the entire wavelength indicating the least absorption in the entire range. For 8%, the transmittance drops below the 4% in the entire range. Therefore, it shows a medium transmittance as compared to the three concentrations. However, in consideration of the percentages, it still shows high transmittance. The 16% showed the lowest transmittance in comparison to the other two doping concentrations. This may be due to increased defect concentration. This may be good for band gap tuning but it may have a challenge in formation of thin films. The graphs also show shift in absorption edge. As sulphur concentration increases, the transmittance of wavelengths below 400 nm (shorter wavelength) decreases more sharply showing redshift or shift towards longer wavelength. It also indicates that impurity states are introduced by sulphur thus reducing the effective band gap of ZnO.

For optoelectronic devices, Figure 4.2 means that higher doping concentration is favorable for tuning band gap and high absorption devices. For the devices that require high transmittance, low doping concentration is necessary. For the case of this research, ZnO:S has been synthesized for electron transport layer, which requires high transmittance and low absorbance. The low doping concentration was preferred. The high transmittance is necessary to allow penetration of solar energy into the perovskite layer which then generate electron hole pairs for perovskite solar cell performance.

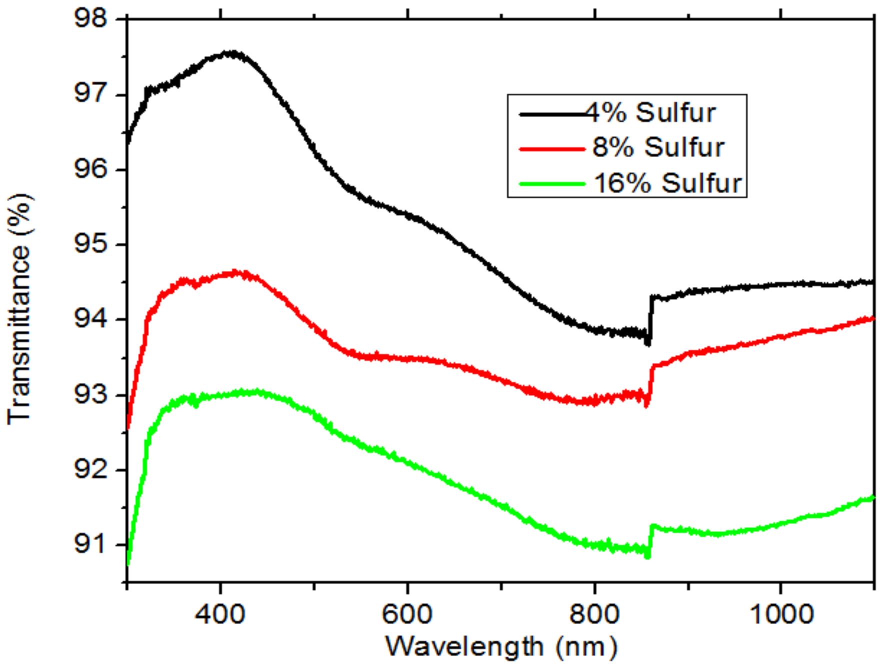

Figure 4.2: Transmission spectrum for ZnO:S at different doping concentrations

Figure 4.3 shows a tauc plot for ZnO:4%S with a band gap of 3.562 eV. On increasing doping concentration to 8, the band gap reduces further to 3.479 eV as shown in Figure 4.4. It therefore means that doping of ZnO with sulphur reduces the band gap of ZnO.

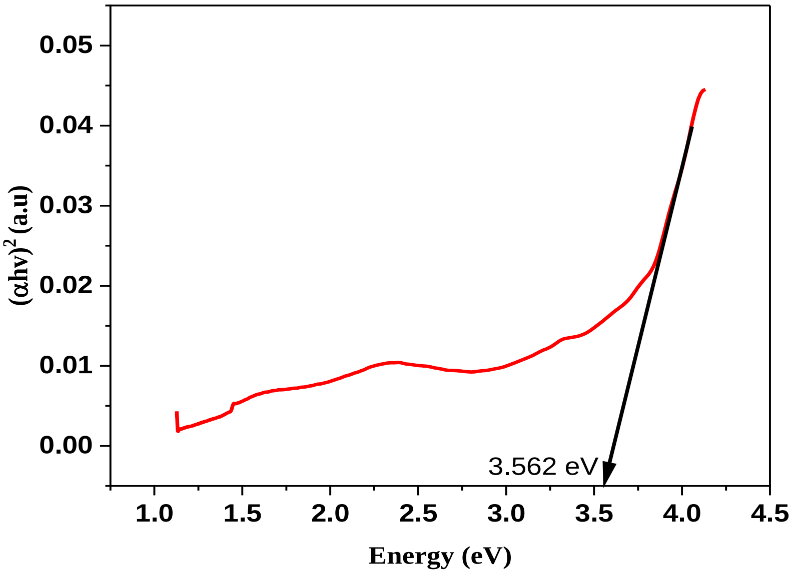

Figure 4.3: Tauc plot for ZnO: 4%S

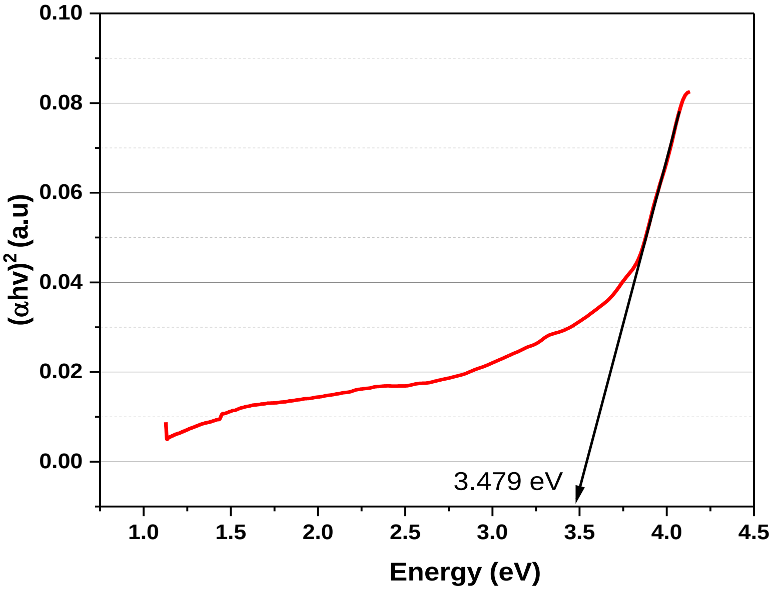

Figure 4.4: Tauc plot for ZnO: 8% S

4.1.3 Morphological Properties of ZnO:S

Figure 4.5 shown SEM images of ZnO:S film doped at different doping concentrations; a) 4 % sulphur doping b) 8 % sulphur doping c) 16 % sulphur doping. The images shown good

ZnO:S films that can be applied in solar cells. They show the surface morphology of three different doping concentrations in ZnO:S. Figure 4.5 (a) depicts densely packed granular texture with very fine surface. The grains seem to be uniformly distributed with almost the same size. This represents well-formed thin film. The homogeneous and smooth interface with less defects shown in the image is desirable for ETL of perovskite solar cell and thus not allowing layers mixing.

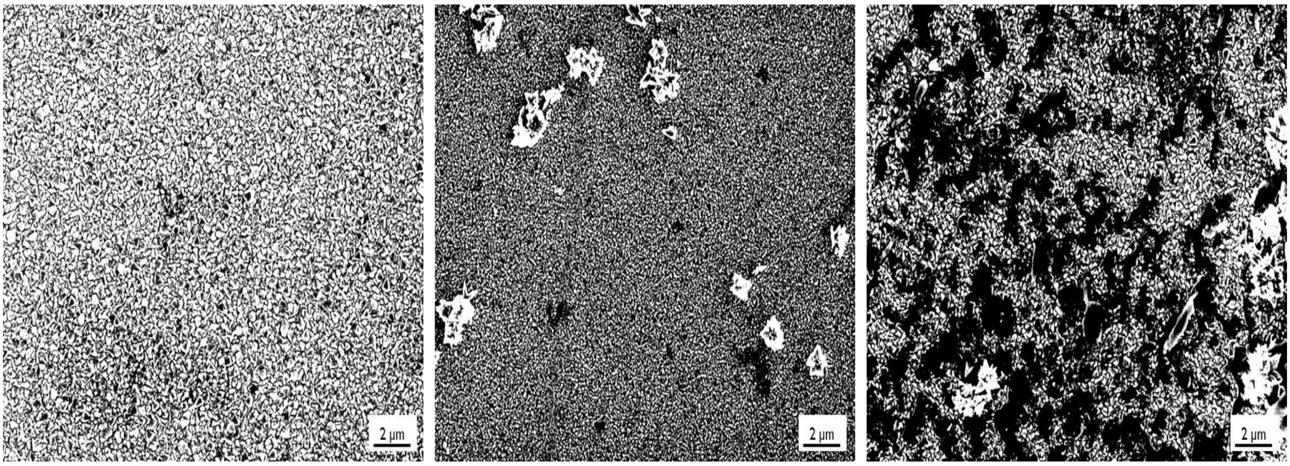

Figure 4.5: SEM images of ZnO:S film doped at different doping concentrations; a) 4 % sulphur doping b) 8 % sulphur doping c) 16 % sulphur doping

Figure 4.5 (b) present different surface morphology. While it still shows granular pattern, it consists of very large particles leading to irregularly shaped clusters. This shows the possibility of agglomeration and impurity of not fully joined into the thin film matrix. Figure 4.5 c) illustrates a surface considerably more heterogeneous compared to first two images. The surface appears rough, large distribution of changing grain sizes and voids of high density with dark regions. This non-uniformity is a noteworthy disadvantage for an ETL material, since it can potentially lead to poor contact with the adjacent perovskite layer, thus increasing the series resistance within the device. The dark areas may signify voids or zones with incomplete material coverage, both of which could severely impair the ETL's function by creating sites for charge recombination and reducing the overall charge extraction efficiency.

Based on the detailed analysis, the SEM images, Figure 4.5 (a) shows the most promising features for ETL in perovskite application. It is uniform with almost defect free surface making it ideal for efficient perovskite solar cells. This would minimize recombination losses and enabling performance consistent with solar cell.

4.1.4: Perovskite Device Fabricated Using ZnO:S Characterization

Using box plot in interpretation, the box represents the interquartile range. The middle 50% of the data is the midpoint between the 25th and 75th percentile. The horizontal line in the box designates the median or 50th percentile of the data. The "whiskers" spread to the minimum and maximum data points within 1.5 times the interquartile range. The points external this range are considered outliers and are shown as individual dots (Mcgill *et al*., 1978; Williamson *et al*., 2018).

Figure 4.6 compares fill factor (FF) with directions (either forward or reversed). Both groups show a similar interquartile range with forward direction showing slightly broader overall spread, with a few lower outliers compared to the reverse direction. The median FF for both forward and reverse directions are nearly identical. Forward median is observed at 58.79% and reverse at 58.76%. From this result, it can be concluded that there is consistency of FF between the two directions in consideration of median with small difference in outliers and variability.

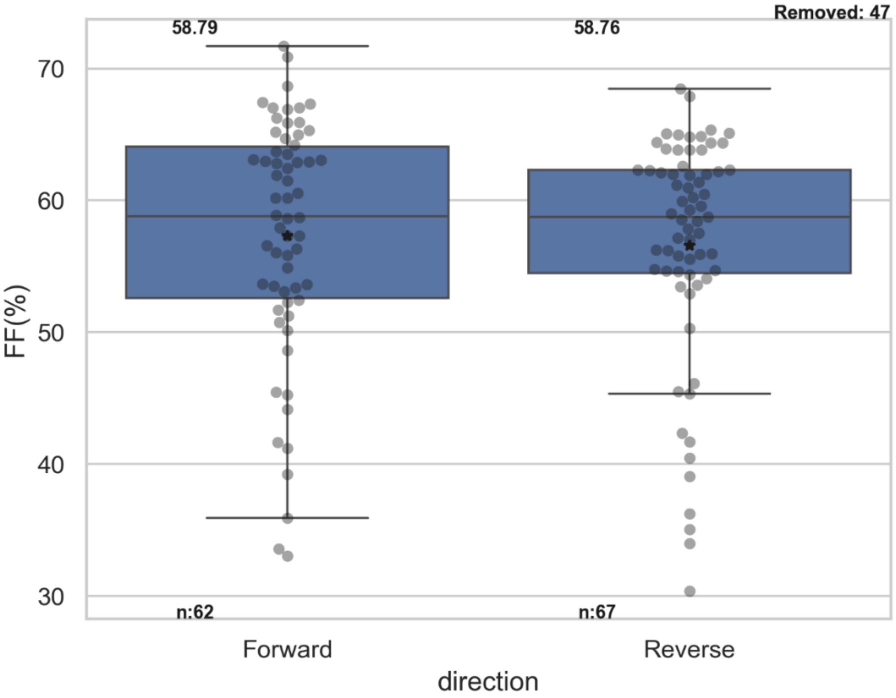

Figure 4.6: Boxplot of FF by direction

Figure 4.7 illustrates how different ETL conditions impact the fill factor of solar device. 4% ZnO:S median FF is around 62.7%, with a moderate spread in the percentile range. 8 % ZnO:S median FF is lower at 56.93%, with a smaller interquartile for reference cell. Its median

FF is the highest at 64.87%, with a narrow spread. Therefore, from Figure 4.9, the reference device is more superior and exhibit a consistent performance; with the highest median FF and least variability. The 4% ZnO:S ETL condition achieves moderately high performance but with increased variability. Conversely, the "8%" condition leads to a significant drop in median FF, suggesting it is less effective in optimizing device performance. These findings highlight the significance of ETL composition in achieving higher FF and improving device performance and reproducibility.

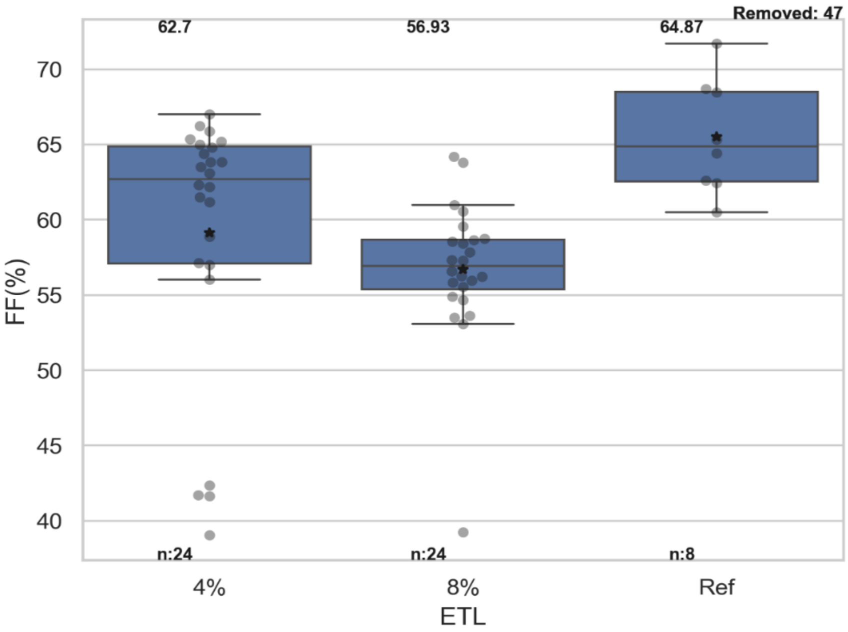

Figure 4.7: Boxplot of FF by ETL at different conditions

Figure 4.8 shows variation between Jsc and direction of biasing. It is observed that there is a minor difference in median values between forward and reverse directions suggesting that the device performance is consistent across different measurement polarities. This is indicative of good device symmetry and stable charge transport under illumination. The presence of outliers, mainly in the reverse direction, may be attributed to fabrication inconsistencies, measurement anomalies and defects. In a nutshell, the plot shows consistent Jscvalues between forward and reverse measurements, with minimal differences in performance. This reinforces the reliability of the fabrication process and device design. Further optimization to reduce outliers could lead to even more robust and reproducible devices.

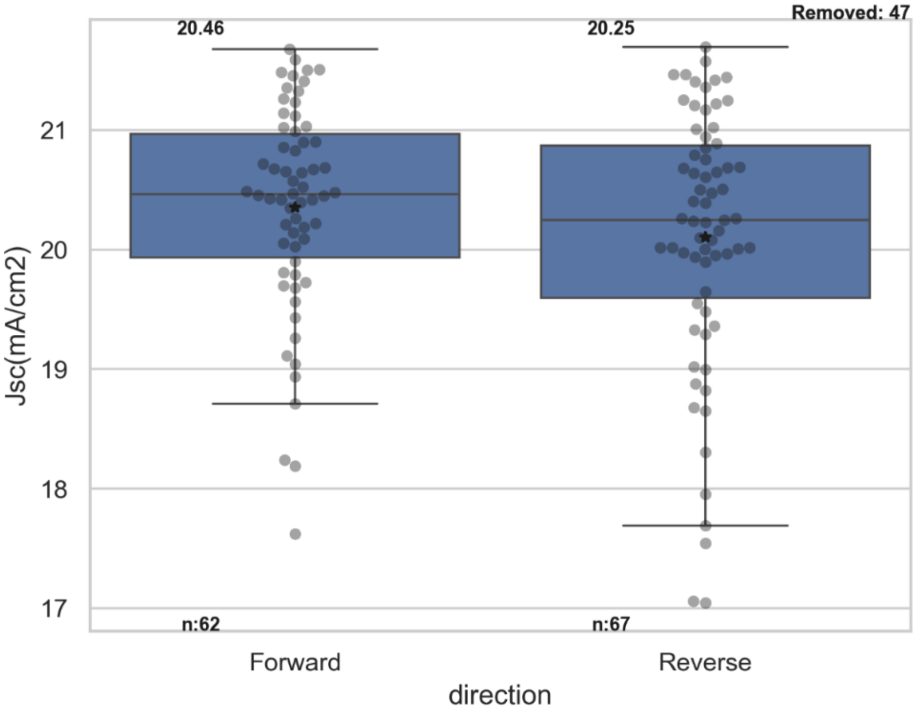

Figure 4.8: Boxplot of Jsc by direction

Figure 4.9 illustrates how different ETL conditions impact the Jsc of devices. The ZnO: 4%S ETL is superior with more consistent Jsc compared to the 8% ETL. This is an indication of lower doping concentration for ETL providing optimal charge transport with reduced losses due to charge recombination. The low performance of ZnO: 8%S ETL might be due to uneven quality of the film and suboptimal thickness leading to increased resistance or defects (Dharmale *et al*., 2024). Therefore, it can be concluded that ZnO: 4%S ETL configuration apparently balances high performance and reasonable reproducibility, making it a promising candidate for future studies.

Figure 4.10 shows a boxplot of PCE (%) in two scan directions. Forward scan indicated a median of approximately 13.09% and reverse scan of approximately 12.48%. It demonstrates that PCE in the forward scan direction is slightly higher than that obtained in the reverse scan, pointing to a moderate hysteresis effect (phenomenon where the I-V curves of the solar cell depend on the speed and the direction of the voltage. This implies that the I-V curve measured during a forward voltage sweep (from short circuit to open circuit) may fluctuate from the curve measured during a reverse voltage sweep (from open circuit to short circuit) (Jena & Miyasaka, 2016). The aforementioned effect is basically due to ionic accumulation and migration in the solar cell, which can lead to measured current densities mismatch (Snaith, 2013). While the efficiency values are very promising, however, the values are too spread.

These variability and hysteresis should be addressed for reproducibility, stable and efficient devices.

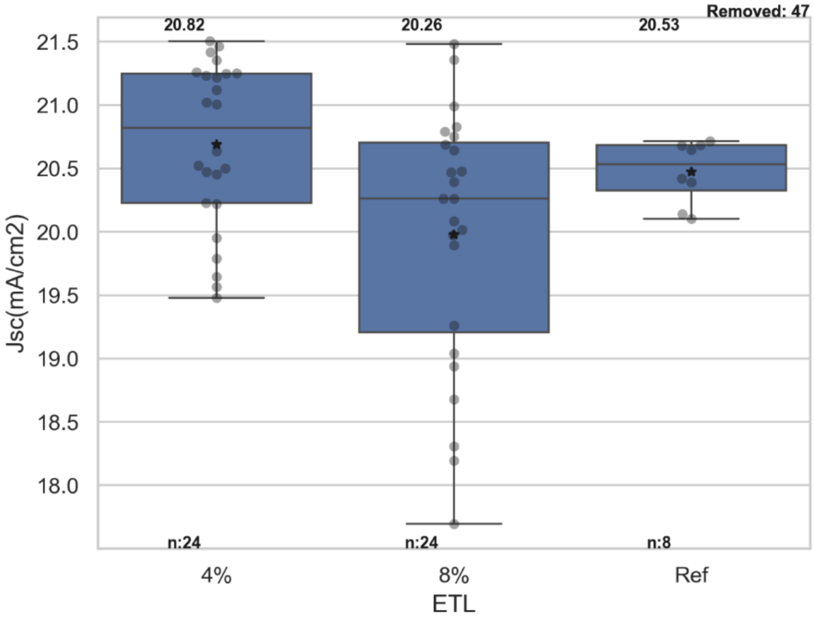

Figure 4.9: Boxplot of Jsc by ETL

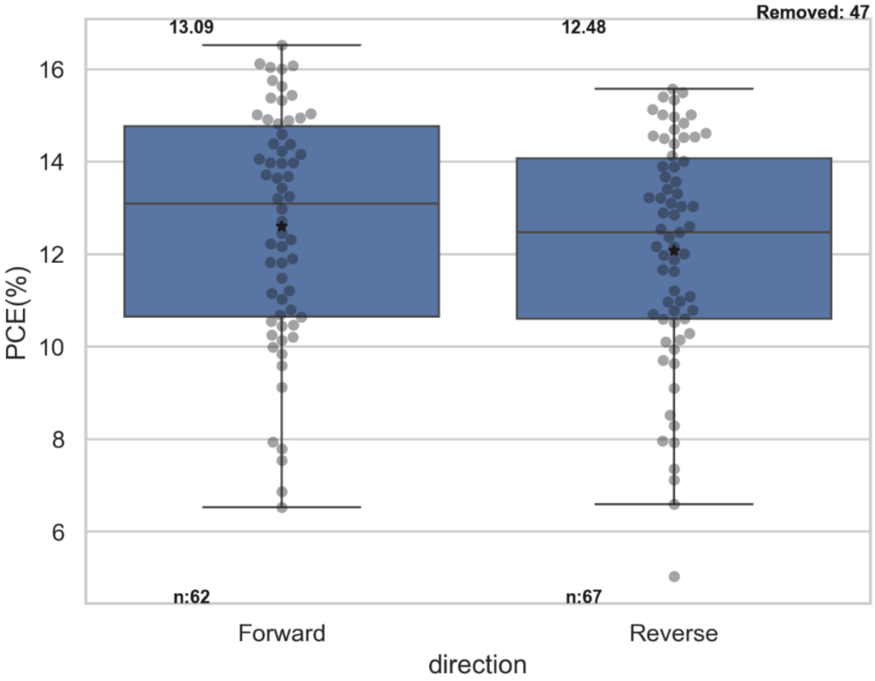

Figure 4.10: Boxplot of PCE by direction

Figure 4.11 shows PCE is impacted by different ETL conditions. The PCE values were 14.55% ZnO: 4% S ETL, 11.94 % ZnO: 8%S ETL and 14.25% for reference devices. There is a significant drop when doping percentage is increased from 4% to 8% ZnO:S ETL, showing that increased in doping introduces detrimental effects like increased charge recombination, poor charge transport, or poor morphology. The reference device demonstrated efficiency very close to that of the ZnO: 4%S ETL but slightly lower, suggesting a pointing to stability and uniformity.

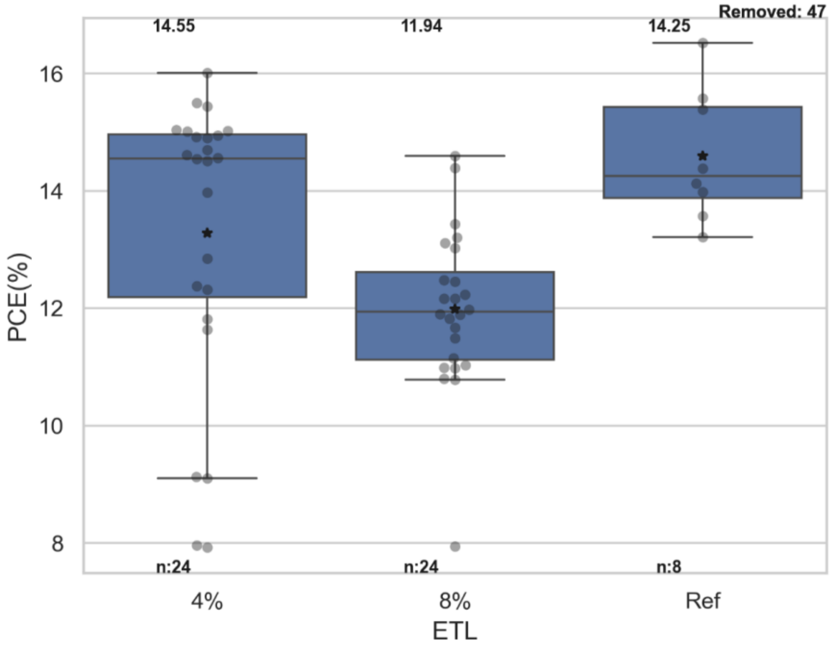

Figure 4.11: Boxplot of PCE by ETL

Figure 4.12 shows the relationship between current density and voltage for a solar cell in forward and reverse directions. Forward directions shown Voc of 1.11 V and reverse Voc of 1.10 V. Their respective Jsc are -20.7 mA/cm² and -20.6 mA/cm². The forward and reverse directions had fill factors of 71.7% and 68.4% respectively. Power conversion efficiency was 16.5% for forward and 15.6% for reverse directions. The difference the two directions are insignificantly small, suggesting negligible hysteresis. This indicates a stable and reproducible device performance. A Voc (above 1 V) and FF (around 75%) means low recombination losses and good contact. Voc above 1.5 V and Jsc of 21 mA/cm points to effective light absorption and charge collection (Van *et al*., 2022). In a nutshell, the sample J-V curves points to efficient photovoltaic behavior, grouped by a high PCE of 16.5% in the forward scan, FF approaching 75%. The minimal hysteresis and strong performance metrics suggest a well-optimized device, making it a promising candidate for perovskite solar cell development.

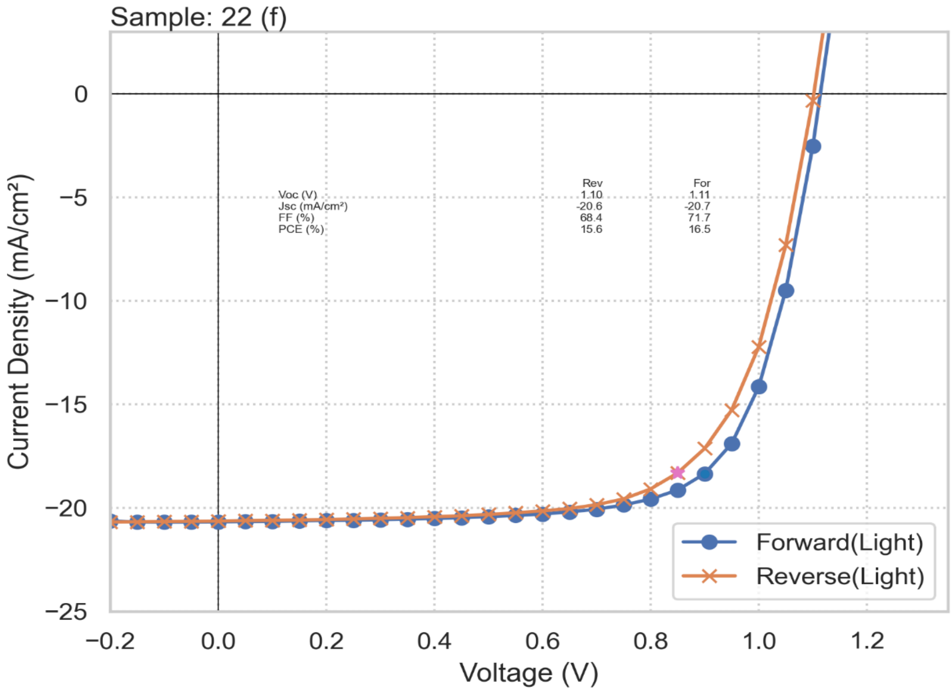

Figure 4.12: J-V characteristics for the best device fabricated with ZnO:S

Figure 4.13 shows stability test for the fabricated solar devices over time. The results suggest that ZnO:8%S ETL has the lowest performance, followed with ZnO:4%S. This results from increased recombination, poor charge transport in higher sulphur content in ZnO ETL. However, on close supervision, the ZnO: 8%S degrades slightly slower than ZnO: 8%S ETL. This implies that even though lower doping concentration has better performance, it decays faster than higher doping concentration. It's also observed that the device shows a better performance both at the beginning and over time. This suggests a well-optimized and less prone to degradation mechanisms in the device compared ZnO:S. Therefore Figure 4.13 suggests that doping increases stability but reduces performance. Future work should focus on optimizing ZnO concentration and mitigating degradation mechanisms to enhance both performance and durability.

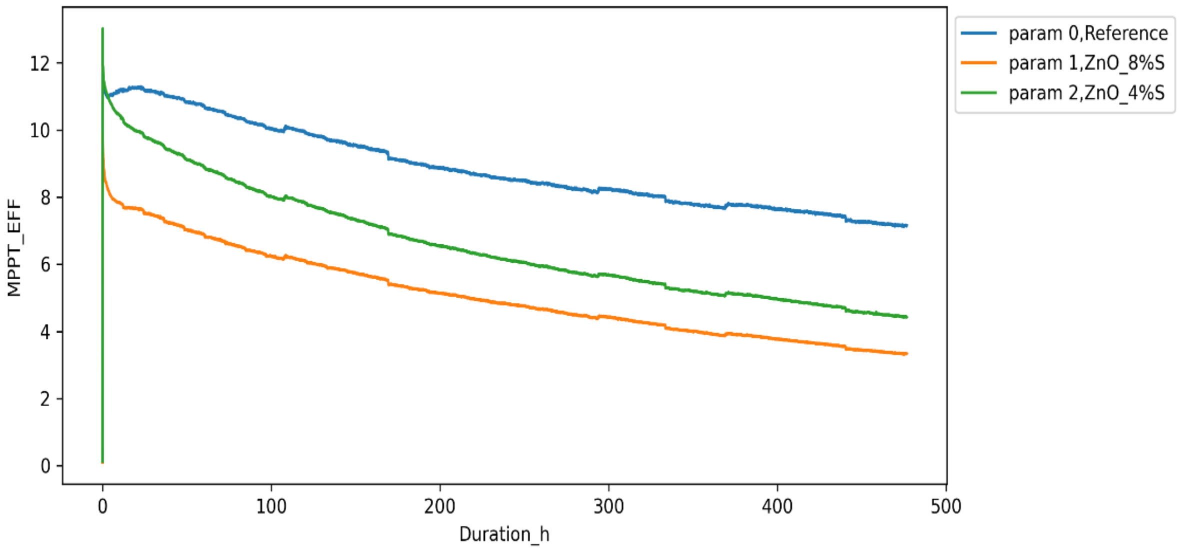

Figure 4.13: Efficiency at maximum power point for fabricated solar devices over time

4.2 $FASnI_2Br$

The characterization of this perovskite material was done and applied in the device.

4.2.1 Structural Properties of FASnI2Br

Figure 4.14 shows the XRD structure of $FASnI_2Br$ synthesized. It gives the general film structure on ZnO film, on clean ITO, and on PEDOT:PSS film. In this case, $FASnI_2Br$ on ZnO film and on PEDOT: PSS film represents n-p-n and p-n-p perovskite device arrangements respectively. The clean ITO substrate shows the general structure of $FASnI_2Br$ perovskite material in absence of any interlayer. The peaks appear around 14°, 24°, 28°, 30.5°, 31°, 36°, 41° and 43° indicating 110, 211, 220, 310, 312, 224 and 314 pattern. When compared with Pure $FASnI_3$, a slight shift towards higher angles due to substitution of large I^- with smaller Br^- ions is observed. The substrates ZnO, ITO, PEDOT influences the intensities of the peak in the $FASnI_2Br$ pattern, suggesting possible interactions or reaction of the film and the substrate (Balvanz *et al*., 2024; Li *et al*., 2018; Ozaki *et al*., 2017).

On a Clean substrate, the film may crystallize more favourably, leading to higher peak intensity. When coated on PEDOT or ZnO, these layers could cause a change in the nucleation and growth processes, resulting in a less preferred orientation or smaller crystallite size, reducing the peak intensity (Han *et al*., 2024). The PEDOT or ZnO might influence the film's coverage and thickness. When the $FASnI_2Br$ layer is thinner on PEDOT or ZnO, this could result in lower XRD peak intensity (Aliaghayee, 2023; Qiu *et al*., 2022).

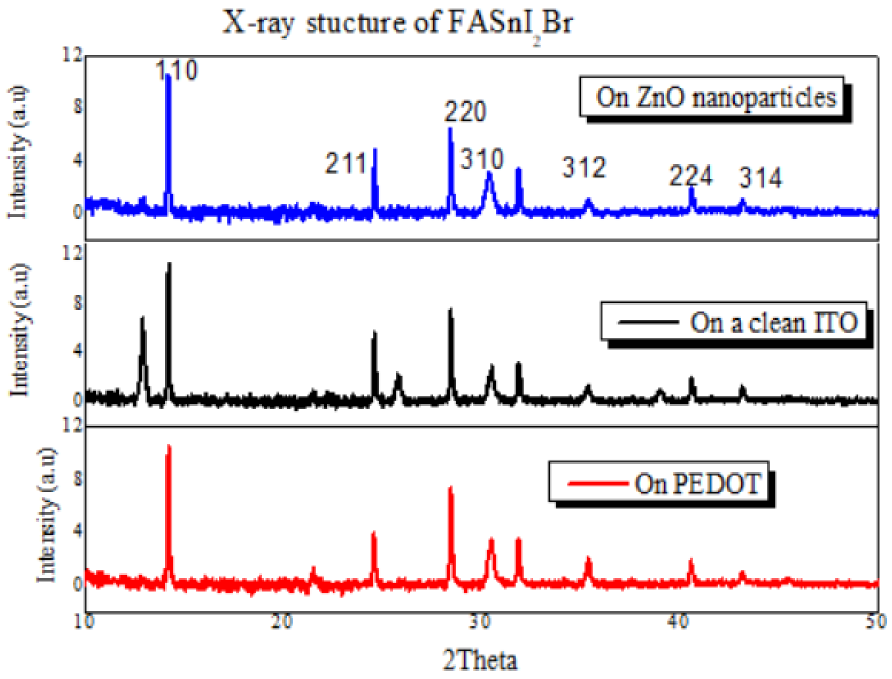

Figure 4.14: X-ray structure of $FASnI_2Br$ on clean FTO, on ZnO, and on PEDOT

4.2.2 Optical Properties of FASnI2Br

Figure 4.15 shows absorption spectra for $FASnI_3$ and $FASnI_2Br$ across 300 nm and 800 nm range for the tin-based perovskite material. $FASnI_3$ shows lower absorption in the range 400 nm and 700nm. It is observed to drop after around 450 nm. This shows that the band gap of $FASnI_3$ is narrow compared to $FASnI_2Br$ which leads to shifting its absorption edge toward longer wavelengths (near-infrared region). The absorbance progressively decreases approaching 800 nm, consistent with the fact that pure iodide perovskites, such as $FASnI_3$, typically exhibit band gaps in the range of 1.4 to 1.6 eV, which corresponds to the absorption edge around 750–850 nm. $FASnI_2Br$, with mixed halides (in this case iodine and bromine), shows higher absorbance through the visible region (300–700 nm), specifically at shorter wavelengths. The enhanced absorption is attributed to the presence of bromine, which introduces a wider band gap. The absorbance in the UV and visible regions is much more prominent, making it an efficient absorber in these ranges. The inclusion of bromine leads to shift of the absorption edge toward shorter wavelengths (also called blue shift). This indicates a wider band gap. The widening of band gap increases the material suitability for higher-energy photons absorption in the UV/blue regions. This is in agreement with reports that showing tuning of band gap in perovskites by halide substitution, with $FASnI_2Br$ having a band gap of around 1.7 to 1.8 eV. $FASnI_2Br$: The mixed halide composition introduces a wider band gap, improved stability and hence reduced tin oxidation challenge, the common problem in tin-based perovskites. Widening of band gap means less absorption in the near-infrared. In the other hand, it results to better performance in the UV and visible regions. These features make $FASnI_2Br$ a very material for single-junction solar cells fabrication, where the primary energy source is ultraviolet-visible light (Kumar *et al.*, 2014; Noel *et al.*, 2014; Shen *et al.*, 2016).

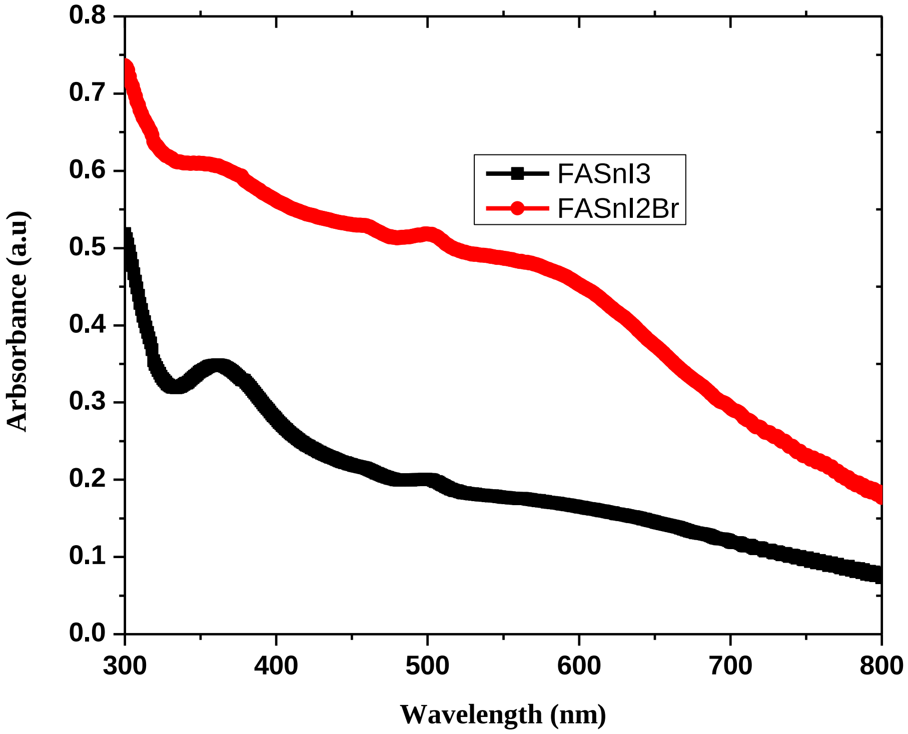

Figure 4.15: Absorption spectrum for $FASnI_3$ and $FASnI_2Br$

4.3 Characterization of Fabricated Solar Device $FASnI_2Br$ Perovskite Material

Figure 4.16 shows a J-V characteristic for a fabricated solar cell device using $FASnI_2Br$ material. The device properties are indicated in the Table 4.1 below. The table 4.1 summarizes the device characteristics information that may not be directly visible on the J-V characteristics and therefore it complements Figure 4.18. It shows solar device parameters. Short-circuit current density (Jsc) shows the current produced per unit area when the terminals of the device are shorted. Jsc for all devices ranges from 11.15 mA/cm² to 12.61 mA/cm² showing light absorption difference. Device A displays the highest Jsc, signifying superior light absorbance capabilities for optimized material as compared to the others. Conversely, device C shows the lowest Jsc, showing a less effective charge carrier generation. Understanding Jsc helps identify the potential for energy production in different solar cell designs.

Open-circuit voltage (Voc) represents the maximum voltage available from a solar cell under open-circuit conditions. The Voc values for the devices range from 0.358 V (Device C) to 0.568 V (Device B). A higher Voc typically indicates a better ability to separate charge carriers and a more favourable energy band structure. Device B not only exhibits the highest Voc but also suggests a potentially higher efficiency in energy conversion due to reduced recombination losses. On the other hand, the lower Voc in Device F may indicate higher recombination rates or material limitations, presence of the defects impacting its overall performance.

Power Conversion Efficiency (PCE) is a metric replicating how effectively a solar device converts sunlight into electrical energy. The PCE values for the devices range from 1.61 % (Device C) to 3.57 % (Device B). Device B stands showing the highest efficiency, likely due to a combination of favourable Jsc, Voc, and FF. In contrast, Device C’s low PCE suggests inefficiencies in both current generation and voltage output. Enhancing PCE is vital for solar technology advancement, and analysing these values assists in identifying the strengths and weaknesses of each device configuration.

Fill Factor (FF) indicates the quality of the solar cell's I-V characteristics and is crucial for understanding overall efficiency. The FF values for these devices were ranging between 40.09 % (Device C) and 50.44 % (Device B). A higher reflects minimal losses and better charge carrier, hence to increased power output. Conversely, the lower FF suggests high series resistance or low shunt resistance, adversely affecting performance. Investigating FF helps in diagnosing and optimizing solar cell design for improved energy conversion efficiency.

The Maximum Power Point (P-MPP) for the devices are consistent with their respective efficiencies, with Device B achieving the highest output of 3.57 mW/cm^2. This result shows the optimal performance of the device across multiple parameters, including Jsc and Voc. In contrast, lower P-MPP of device C indicates a less effective energy conversion capability. Hence the importance of optimizing the contributing factors for power output maximization in solar applications.

Series resistance (Rser) and shunt resistance (Rsh) are factors affecting the efficiency of solar cells. Rser values range from 0.0104 Ωcm to 0.0167 Ωcm, with lower values showing good conductivity and less losses. Low series resistance of Device B correlates with its high FF and PCE, suggesting efficient charge transport. Conversely, the higher series resistance in Device E may lead to increased energy losses due to charge carrier recombination.

Shunt resistance (Rsh) varies from 0.098 Ωcm (Devices C and E) to 0.283 Ωcm (Device A). Higher the shunt resistance the better the cell indicating fewer leakage and better overall efficiency. By analysing these resistances, researchers can better understand the limitations and areas for improvement in solar cell design and functionality.

Table 4.1: Fabricated solar device parameters with ZnO:S ETL and $FASnI_2Br$ active layer

Device property	A	B	C	D	E	F
Jsc (mA/cm^2)	12.60712	12.46156	11.23699	11.15283	11.24476	11.16323
Voc (V)	0.438967	0.567852	0.358196	0.442232	0.447346	0.501859
PCE (%)	2.551215	3.569629	1.613746	2.045414	2.057007	2.331215
FF (%)	46.099821	50.444634	40.092608	41.471121	40.892349	41.611280
P-MPP (mW/cm^2)	2.551215	3.569629	1.613746	2.045414	2.057007	2.331215
J-MPP (mA/cm^2)	-9.448944	-8.706411	-7.684506	-7.053150	-7.618544	-7.064289
U MPP (V)	0.270000	0.410000	0.210000	0.290000	0.270000	0.330000
R Ser (Ωcm)	0.012917	0.010433	0.013962	0.013903	0.016672	0.01426
R Sh (Ωcm)	0.283191	0.151935	0.098109	0.097260	0.120805	0.098210

The current density-voltage (J-V) characteristics of photovoltaic devices shows information valuable on their performance, such as efficiency, fill factor, open-circuit voltage (Voc), and short-circuit current density (Jsc). From Figure 4.16; the following observations were made. Device B had the highest current density, followed by A. Thus, they represent top performing cells in this set of devices. C to E have medium performance. Device F represent the poorest performing device having least current density and predictively very high losses due to charge recombination. Device B shows slightly higher open circuit voltage and device F shows slightly lower open circuit voltage. On observing the curves for the fill factor, the J-V shapes near the maximum power point can give insight on the fill factor. B has the highest fill factor. This is in agreement with good charge extraction as well as lower series resistance. Devices D and E comparatively flattens and hence showing lower FF because higher series resistance and effects of shunting.

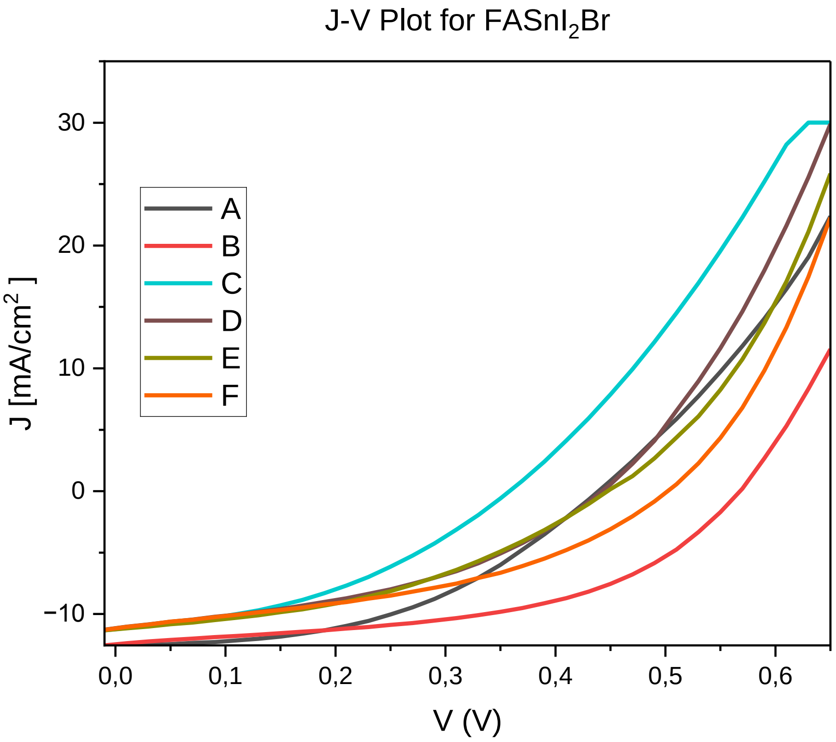

Figure 4.16: J-V characteristics for six devices fabricated with FASnI$_2$Br

CHAPTER FIVE

SUMMARY, CONCLUSIONS AND RECOMMENDATIONS

5.1 Summary

This study focused on improving the existing materials for perovskite solar cells by synthesizing ZnO:S and $FASnI_2Br$ for ETL and perovskite material in that order. The resultant materials were characterised for structural and optoelectrical properties using X-ray diffraction and UV-vis spectroscopy methods respectively. It was concluded that doping of ZnO with sulphur leads to band gap narrowing. Increase in sulphur doping concentration reduced transmission thus higher doping concentration may not be necessary for ETL of perovskite solar devices since a good ETL requires a wideband gap and high transmittance. In this study, ZnO: 4 %S is the preferred for ETL. Similarly, ZnO:S was found to form wurtzite hexagonal structure with new peaks depicting peaks of sulphur. Additionally, the structure of $FASnI_2Br$ is similar to that of perovskite materials. $FASnI_2Br$ has a wider band gap compared to $FASnI_3$. This leads to improved optical absorbance of $FASnI_2Br$. And since perovskite material should have higher absorbance, increased optical absorbance of $FASnI_2Br$ best suited over $FASnI_3$. For the devices fabricated with ZnO:S indicated a good performance and stability. The performance of the devices using ZnO: 4 %S ETL were a PCE of 16.5%, Jsc of 21.3 $mAcm^{-2}$ and Voc of 1.15 V when tested using $FAPbI_3$. For the devices fabricated using $FASnI_2Br$, moderate performance was obtained. Best performing device had a PCE of 3.57%, Voc of 0.569V and Jsc of 0.568 $mAcm^{-2}$.

5.2 Conclusions

From this research, the following conclusions were made:

i. $FASnI_2Br$ and ZnO:S was successfully synthesised using solution-based method for device application.
ii. The structural properties of $FASnI_2Br$ and ZnO:S were successfully determined using X-ray diffraction. $FASnI_2Br$ shown a perovskite structure and ZnO:S a wurtzite hexagonal structure.
iii. The optical properties of $FASnI_2Br$ and ZnO:S were successfully determined using UV-Vis spectroscopy. $FASnI_2Br$ and ZnO:S shown improved absorption and transmittance respectively. On the other hand $FASnI_2Br$ indicated increased band gap and ZnO:S a reduction in band gap.
iv. Perovskite solar cells were successfully fabricated and characterized using $FASnI_2Br$ and ZnO:S. Upto a PCE of 16.5 % was obtained for the ZnO:S ETL and PCE of 3.57

% for $FASnI_2Br$. However, the two materials were not compatible and could not perform on one device.

5.3 Recommendations

To improve solar device performance, this study recommends the following directions for the future research.

i. Investigate synthesis of $FASnI_2Br$ at different mole ratios of iodine and bromine.
ii. Implement the use of temperature dependent X-ray diffraction (TXRD) for Phase evolution and thermal stability analysis of $FASnI_2Br$ and ZnO:S.
iii. Investigate how the interface and surface properties can be used to enhance optoelectronic properties of the synthesised $FASnI_2Br$ and ZnO:S.
iv. Explore interfacial passivation materials between $FASnI_2Br$ and ZnO:S using very thin layers such as self-assembled monolayers and Al_2O_3.

5.4 Suggestions for Further Studies

This research gives the following as suggestions for future study on this area.

i. Study on in-situ monitoring of tin oxidation from Sn2+ to Sn4+ during synthesis of $FASnI_2Br$ and film formation using in-situ XPS or any other available equipment
ii. Study how partial substitution of FA+ with MA^+ or Cs can enhance stability and fine tune band gap of $FASnI_2Br$.
iii. Study on different methods of preparation of ZnO:S such as hydrothermal, sol gel, precipitation, spray pyrolysis and RF magnetron sputtering methods and choose on the best for perovskite solar.
iv. Perform a study on additives that will allow fabrication of solar device using $FASnI_2Br$ and ZnO:S simultaneously.
v. Perform a study on other materials such as HTL, other ETL materials, and electrode materials to be used for fabrication of perovskite solar cells using the synthesised $FASnI_2Br$, ZnO:S and when both are used simultaneously. Compare their performance.

REFERENCES

Abidin, N. A., Arith, F., Noorasid, N. S., Sarkawi, H., Mustafa, A. N., Safie, N. E., Shah, A. S., Azam, M. A., Chelvanathan, P., & Amin, N. (2023). Dopant engineering for ZnO electron transport layer towards efficient perovskite solar cells. *RSC Advances*, 13(48), 33797-33819. https://doi.org/10.1039/d3ra04823c

Aftab, A., & Ahmad, M. I. (2021). A review of stability and progress in tin halide perovskite solar cell. *Solar Energy*, 216(1), 26-47. https://doi.org/10.1016/j.solener.2020.12.065

Akash, M. S., & Rehman, K. (2020). *Ultraviolet-visible (UV-Vis) spectroscopy*. *Essentials of Pharmaceutical Analysis*, 29-56. https://doi.org/10.1007/978-981-15-1547-7_3

Akman, E., Shalan, A. E., Sadegh, F., & Akin, S. (2021). Moisture-resistant FAPbI₃ perovskite solar cell with 22.25 % power conversion efficiency through Pentafluorobenzyl Phosphonic acid Passivation. *ChemSusChem*, *14*(4), 1176-1183. https://doi.org/10.1002/cssc.202002707

Ali, A., Chiang, Y. W., & Santos, R. M. (2022). X-ray diffraction techniques for mineral characterization: A review for engineers of the fundamentals, applications, and research directions. *Minerals*, *12*(2), 205. https://doi.org/10.3390/min12020205

Aliaghayee, M. (2023). Optimization of the perovskite solar cell design with layer thickness engineering for improving the photovoltaic response using SCAPS-1D. *Journal of Electronic Materials*, *52*(4), 2475-2491. https://doi.org/10.1007/s11664-022-10203-x

Asare, J., Sanni, D. M., Agyei-Tuffour, B., Agede, E., Oyewole, O. K., Yerramilli, A. S., & Doumon, N. Y. (2021). A hybrid hole transport layer for perovskite-based solar cells. *Energies*, *14*(7), 1949. https://doi.org/10.3390/en14071949

Asghar, M., Zhang, J., Wang, H., & Lund, P. (2017). Device stability of perovskite solar cells – A review. *Renewable and Sustainable Energy Reviews*, *77*, 131-146. https://doi.org/10.1016/j.rser.2017.04.003

Baird, I. G., Silvano, R. A., Parlee, B., Poesch, M., Maclean, B., Napoleon, A., Lepine, M., & Hallwass, G. (2021). The downstream impacts of hydropower dams and Indigenous and local knowledge: Examples from the Peace–Athabasca, Mekong, and Amazon. *Environmental Management*, *67*(4), 682-696. https://doi.org/10.1007/s00267-020-01418-x

Balvanz, A., Safdari, M., Zacharias, M., Kim, D., Welton, C., Oriel, E. H., Kepenekian, M., Katan, C., Malliakas, C. D., Even, J., Klepov, V., Manjunatha Reddy, G. N., Schaller, R. D., Chen, L. X., Seshadri, R., & Kanatzidis, M. G. (2024). Structural evolution and photoluminescence quenching across the fasni<sub>3–

x</sub>Br_{<i>x</i>} (<i>x</i> = 0–3) perovskites. *Journal of the American Chemical Society*, *146*(23), 16128-16147. https://doi.org/10.1021/jacs.4c03669

Beygisangchin, M., Kamarudin, S. K., Umar, A. A., Farhadi, B., Baghdadi, A. H., Letchumanan, I., Rajabi, A., Ehsan, A. A., & Shaari, N. (2024). Advancements in configuration structures and fabrication techniques for achieving stability in perovskite solar cells: A comprehensive review. *Journal of the Korean Ceramic Society*, *61*(5), 755-782. https://doi.org/10.1007/s43207-024-00401-0

Bonadio, A., Escanhoela, C. A., Sabino, F. P., Sombrio, G., De Paula, V. G., Ferreira, F. F., Janotti, A., Dalpian, G. M., & Souza, J. A. (2021). Entropy-driven stabilization of the cubic phase of MaPbI₃ at room temperature. *Journal of Materials Chemistry A*, *9*(2), 1089-1099. https://doi.org/10.1039/d0ta10492b

Cai, T., Shi, W., Hwang, S., Kobbekaduwa, K., Nagaoka, Y., Yang, H., Hills-Kimball, K., Zhu, H., Wang, J., Wang, Z., Liu, Y., Su, D., Gao, J., & Chen, O. (2020). Lead-free $Cs_4CuSb_2Cl_{12}$ layered double perovskite Nanocrystals. *Journal of the American Chemical Society*, *142*(27), 11927-11936. https://doi.org/10.1021/jacs.0c04919

Calado, P., Telford, A. M., Bryant, D., Li, X., Nelson, J., O'Regan, B. C., & Barnes, P. R. (2016). Evidence for ion migration in hybrid perovskite solar cells with minimal hysteresis. *Nature Communications*, *7*(1). https://doi.org/10.1038/ncomms13831

Chakkamalayath, J., Hartland, G. V., & Kamat, P. V. (2022). Photoinduced transformation of $Cs_2Au_2Br_6$ into $CsPbBr_3$ Nanocrystals. *The Journal of Physical Chemistry Letters*, *13*(13), 2921-2927. https://doi.org/10.1021/acs.jpclett.2c00473

Chawla, R., Singhal, P., & Garg, A. K. (2020). Photovoltaic review of all generations: Environmental impact and its market potential. *Transactions on Electrical and Electronic Materials*, *21*(5), 456-476. https://doi.org/10.1007/s42341-020-00217-9

Chen, L., & Tseng, Z. (2017). *Zno-based electron transporting layer for perovskite solar cells*. *Nanostructured Solar Cells*. https://doi.org/10.5772/65056

Chen, W., Zhu, Y., Yu, Y., Xu, L., Zhang, G., & He, Z. (2016). Low cost and solution processed interfacial layer based on Poly(2-Ethyl-2-oxazoline) Nanodots for inverted perovskite solar cells. *Chemistry of Materials*, *28*(14), 4879-4883. https://doi.org/10.1021/acs.chemmater.6b00964

Chen, Z., & Dhakal, T. P. (2023). Room temperature synthesis of lead-free FASnI3 perovskite nanocrystals with improved stability by SnF2 additive. *Applied Physics Reviews*, *10*(1). https://doi.org/10.1063/5.0125100

Coulibaly, A. B., Oyedele, S. O., Kre, N. R., & Aka, B. (2019). Comparative study of lead-free perovskite solar cells using different hole transporter materials. *Modeling and Numerical Simulation of Material Science*, *09*(04), 97-107. https://doi.org/10.4236/mnsms.2019.94006

Dai, T., Cao, Q., Yang, L., Aldamasy, M., Li, M., Liang, Q., Lu, H., Dong, Y., & Yang, Y. (2021). Strategies for high-performance large-area perovskite solar cells toward commercialization. *Crystals*, *11*(3), 295. https://doi.org/10.3390/cryst11030295

Dharmale, N., A, A., Srivastava, A., & Chaudhury, S. (2024). *Journal of Molecular Modeling*, *30*(5). https://doi.org/10.1007/s00894-024-05943-y

Domanski, K., Correa-Baena, J., Mine, N., Nazeeruddin, M. K., Abate, A., Saliba, M., Tress, W., Hagfeldt, A., & Grätzel, M. (2016). Not all that glitters is gold: Metal-migration-Induced degradation in perovskite solar cells. *ACS Nano*, *10*(6), 6306-6314. https://doi.org/10.1021/acsnano.6b02613

Du, H., Wang, W., & Zhu, J. (2016). Device simulation of lead-free CH ₃ NH ₃ SnI ₃ perovskite solar cells with high efficiency. *Chinese Physics B*, *25*(10), 108802. https://doi.org/10.1088/1674-1056/25/10/108802

Duan, Y., Wang, J., Xu, D., Ji, P., Zhou, H., Li, Y., ... & Liu, Z. (2024). 21.41%-Efficiency CsPbI3 Perovskite Solar Cells Enabled by an Effective Redox Strategy with 4-Fluorobenzothiohydrazide in Precursor Solution. *Advanced Functional Materials*, *34*(10), 2312638. https://doi.org/10.1002/adfm.202312638

Esmaeili, F., & Khosroabadi, S. (2021). A novel design of high efficiency perovskite solar cell using electron reflector strategy and transport layers optimization. *The European Physical Journal Plus*, *136*(9). https://doi.org/10.1140/epjp/s13360-021-01794-1

Fakharuddin, A., De Rossi, F., Watson, T. M., Schmidt-Mende, L., & Jose, R. (2017). Research update: Behind the high efficiency of hybrid perovskite solar cells. *APL Materials*, *4*(9). https://doi.org/10.1063/1.4962143

Gamal, N., Sedky, S. H., Shaker, A., & Fedawy, M. (2021). Design of lead-free perovskite solar cell using zn1-mg O as ETL: SCAPS device simulation. *Optik*, *242*, 167306. https://doi.org/10.1016/j.ijleo.2021.167306

Gao, Y., Wu, Y., Lu, H., Chen, C., Liu, Y., Bai, X., Yang, L., Yu, W. W., Dai, Q., & Zhang, Y. (2019). CsPbBr3 perovskite nanoparticles are an additive for environmentally stable perovskite solar cells with 20.46% efficiency. *Nano Energy*, *59*, 517-526. https://doi.org/10.1016/j.nanoen.2019.02.070

Giustino, F., & Snaith, H. J. (2016). Toward lead-free perovskite solar cells. *ACS Energy Letters*, *1*(6), 1233-1240. https://doi.org/10.1021/acsenergylett.6b00499

Guarnera, S., Abate, A., Zhang, W., Foster, J. M., Richardson, G., Petrozza, A., & Snaith, H. J. (2015). Improving the long-term stability of perovskite solar cells with a porous Al₂O₃ buffer layer. *The Journal of Physical Chemistry Letters*, *6*(3), 432-437. https://doi.org/10.1021/jz502703p

Gupta, S., Cahen, D., & Hodes, G. (2018). How SnF₂ impacts the material properties of lead-free tin perovskites. *The Journal of Physical Chemistry C*, *122*(25), 13926-13936. https://doi.org/10.1021/acs.jpcc.8b01045

Han, C., Wang, M., & Jeong, H. (2024). Effects of crystal orientation, substrate type, and substrate temperature on residual stress of AlN thin films deposited by different deposition methods. *Journal of the Korean Physical Society*, *84*(7), 538-549. https://doi.org/10.1007/s40042-024-01008-8

Howard, I. A., Abzieher, T., Hossain, I. M., Eggers, H., Schackmar, F., Ternes, S., Richards, B. S., Lemmer, U., & Paetzold, U. W. (2019). Coated and printed perovskites for photovoltaic applications. *Advanced Materials*, *31*(26). https//doi.org/10.1002/adma.201806702

Hu, X., Li, J., Wang, C., Cui, H., Liu, Y., Zhou, S., Guan, H., Ke, W., Tao, C., & Fang, G. (2023). Antimony potassium tartrate stabilizes wide-bandgap perovskites for inverted 4-T all-perovskite tandem solar cells with efficiencies over 26%. *Nano-Micro Letters*, *15*(1). https://doi.org/10.1007/s40820-023-01078-6

Jena, A. K., & Miyasaka, T. (2016). *Organic-Inorganic Halide Perovskite Photovoltaics*, 255-284. https://doi.org/10.1007/978-3-319-35114-8_10

Jeong, D., Lee, D., Seo, S., Lim, S. Y., Zhang, Y., Shin, H., Cheong, H., & Park, N. (2019). Perovskite cluster-containing solution for scalable D-bar coating toward high-throughput perovskite solar cells. *ACS Energy Letters*, *4*(5), 1189-1195. https://doi.org/10.1021/acsenergylett.9b00042

Jeong, J., Kim, M., Seo, J., Lu, H., Ahlawat, P., Mishra, A., Yang, Y., Hope, M. A., Eickemeyer, F. T., Kim, M., Yoon, Y. J., Choi, I. W., Darwich, B. P., Choi, S. J., Jo, Y., Lee, J. H., Walker, B., Zakeeruddin, S. M., Emsley, L., … Kim, J. Y. (2021).

Jia, J., Wu, J., Dong, J., Fan, L., Huang, M., Lin, J., & Lan, Z. (2018). Cadmium sulfide as an efficient electron transport material for inverted planar perovskite solar cells. *Chemical Communications*, *54*(25), 3170-3173. https://doi.org/10.1039/c7cc09838c

Kajal, P., Ghosh, K., & Powar, S. (2018). *Manufacturing techniques of perovskite solar cells.* Applications of Solar Energy, 341-364. https://doi.org/10.1007/978-981-10-7206-2_16

Kanoun, A., Kanoun, M. B., Merad, A. E., & Goumri-Said, S. (2019). Toward development of high-performance perovskite solar cells based on $CH_3NH3GeI_3$ using computational approach. *Solar Energy*, *182*, 237-244. https://doi.org/10.1016/j.solener.2019.02.041

Katila, P., Pierce Colfer, C. J., Jong, W. D., Galloway, G., Pacheco, P., & Winkel, G. (2019). Introduction. *Sustainable Development Goals: Their Impacts on Forests and People*, 1-16. https://doi.org/10.1017/9781108765015.002

Kato, Y., Ono, L. K., Lee, M. V., Wang, S., Raga, S. R., & Qi, Y. (2015). Silver iodide formation in methyl ammonium lead iodide perovskite solar cells with silver top electrodes. *Advanced Materials Interfaces*, *2*(13). https://doi.org/10.1002/admi.201500195

Kareem, H. S., Harjan Elewi, M., Muhson Naji, A., Ahmed, D. S., & K. A. Mohammed, M. (2022). Efficient and stable pure α-phase FAPbI3 perovskite solar cells with a dual engineering strategy: Additive and dimensional engineering approaches. *Chemical Engineering Journal*, *443*, 136469. https://doi.org/10.1016/j.cej.2022.136469

Kim, J. H., Williams, S. T., Cho, N., Chueh, C., & Jen, A. K. (2015). Enhanced environmental stability of planar Heterojunction perovskite solar cells based on blade-coating. *Advanced Energy Materials*, *5*(4). https://doi.org/10.1002/aenm.201401229

Konstantakou, M., & Stergiopoulos, T. (2017). A critical review on tin halide perovskite solar cells. *Journal of Materials Chemistry A*, *5*(23), 11518-11549. https://doi.org/10.1039/c7ta00929a

Kumar, S., Aftab, A., & Ahmad, M. I. (2020). Compact Titania films by spray pyrolysis for application as ETL in perovskite solar cells. *Journal of Electronic Materials*, *49*(12), 7159-7167. https://doi.org/10.1007/s11664-020-08464-5

Lamas, D. G., De Oliveira Neto, M., Kellermann, G., & Craievich, A. F. (2017). *X-ray diffraction and scattering by nanomaterials.* Nanocharacterization Techniques, 111-182. https://doi.org/10.1016/b978-0-323-49778-7.00005-9

Lee, K., Chiu, W., Tsai, Y., Wang, C., Tao, Y., & Lin, Y. (2022). High-performance perovskite solar cells based on dopant-free hole-transporting material fabricated by a thermal-assisted blade-coating method with efficiency exceeding 21%. *Chemical Engineering Journal*, *427*, 131609. https://doi.org/10.1016/j.cej.2021.131609

Lee, M. (2017). *X-ray diffraction for materials research*. https://doi.org/10.1201/b19936

Leijtens, T., Eperon, G. E., Pathak, S., Abate, A., Lee, M. M., & Snaith, H. J. (2013). Overcoming ultraviolet light instability of sensitized TiO2 with meso-superstructured organometal tri-halide perovskite solar cells. *Nature Communications*, *4*(1). https://doi.org/10.1038/ncomms3885

Leijtens, T., Prasanna, R., Gold-Parker, A., Toney, M. F., & McGehee, M. D. (2017). Mechanism of tin oxidation and stabilization by lead substitution in tin halide perovskites. *ACS Energy Letters*, *2*(9), 2159-2165. https://doi.org/10.1021/acsenergylett.7b00636

Li, F., & Liu, M. (2017). Recent efficient strategies for improving the moisture stability of perovskite solar cells. *Journal of Materials Chemistry A*, *5*(30), 15447-15459. https://doi.org/10.1039/c7ta01325f

Li, X., Liu, X., Li, Y., Gao, D., & Cao, L. (2021). Using novel semiconductor features to construct advanced ZnO nanowires-based ultraviolet Photodetectors: A brief review. *IEEE Access*, *9*, 11954-11973. https://doi.org/10.1109/access.2021.3051187

Li, Z., & Aik Khor, K. (2018). *Preparation and properties of coatings and thin films on metal implants*. *Encyclopedia of Biomedical Engineering*, 203-212. https://doi.org/10.1016/b978-0-12-801238-3.11025-6

Li, X., Chen, Y., Li, L., & Huang, J. (2018). Perovskite thin film consisting with one-dimensional Nanowires. *Materials*, *11*(9), 1759. https://doi.org/10.3390/ma11091759

Lin, Y., Li, T., Liu, Y., Bahrami, B., Guo, D., Fang, Y., Shao, Y., Chowdhury, A. H., Wang, Q., Deng, Y., Gruverman, A., Savenije, T. J., Qiao, Q., & Huang, J. (2021). Perovskite solar cells with embedded homojunction via nonuniform metal ion doping. *Cell Reports Physical Science*, *2*(5), 100415. https://doi.org/10.1016/j.xcrp.2021.100415

Madriaga, V. G., Rossa, V., Ferreira, L. E., Da Costa Vasconcelos, S., & Lima, T. M. (2023). *Key limitations of biomass-derived carbon Nanostructures for energy application*. *Biomass-Based Functional Carbon Nanostructures for Supercapacitors*, 75-97. https://doi.org/10.1007/978-981-99-0996-4_3

Marcos, C. (2022). *Methods and applications of X-ray diffraction in crystallography and mineralogy*. *Springer Textbooks in Earth Sciences, Geography and Environment*, 383-436. https://doi.org/10.1007/978-3-030-96783-3_17

Marković, S., Stojković Simatović, I., Ahmetović, S., Veselinović, L., Stojadinović, S., Rac, V., Škapin, S. D., Bajuk Bogdanović, D., Janković Častvan, I., & Uskoković, D. (2019). Surfactant-assisted microwave processing of ZnO particles: A simple way for designing the surface-to-bulk defect ratio and improving photo (electro)catalytic properties. *RSC Advances*, *9*(30), 17165-17178. https://doi.org/10.1039/c9ra02553g

Mattaparthi, S., Sinha, D. K., Bhura, A., & Khosla, R. (2023). Design of an eco-friendly perovskite AU/NIO/FASnI3/ZnO0.25S0.75/FTO, device structure for solar cell applications using SCAPS-1D. *Results in Optics*, *12*, 100444. https://doi.org/10.1016/j.rio.2023.100444

McGill, R., Tukey, J. W., & Larsen, W. A. (1978). Variations of box plots. *The American Statistician*, *32*(1), 12. https://doi.org/10.2307/2683468

Milichko, V. A., Shalin, A. S., Mukhin, I. S., Kovrov, A. E., Krasilin, A. A., Vinogradov, A. V., Belov, P. A., & Simovski, C. R. (2016). Solar photovoltaics: Current state and trends. *Physics-Uspekhi*, *59*(8), 727-772. https://doi.org/10.3367/ufne.2016.02.037703

Mohammed, M. K., Dehghanipour, M., Younis, U., Shalan, A. E., Sakthivel, P., Ravi, G., Bhoite, P. H., & Pospisil, J. (2020). Improvement of the interfacial contact between zinc oxide and a mixed cation perovskite using carbon nanotubes for ambient-air-processed perovskite solar cells. *New Journal of Chemistry*, *44*(45), 19802-19811. https://doi.org/10.1039/d0nj04656f

Nath, D., Singh, F., & Das, R. (2020). X-ray diffraction analysis by Williamson-hall, Halder-Wagner and size-strain plot methods of CdSe nanoparticles- a comparative study. *Materials Chemistry and Physics*, *239*, 122021. https://doi.org/10.1016/j.matchemphys.2019.122021

Nishimura, K., Kamarudin, M. A., Hirotani, D., Hamada, K., Shen, Q., Iikubo, S., Minemoto, T., Yoshino, K., & Hayase, S. (2020). Lead-free tin-halide perovskite solar cells with 13% efficiency. *Nano Energy*, *74*, 104858. https://doi.org/10.1016/j.nanoen.2020.104858

Noel, N. K., Abate, A., Stranks, S. D., Parrott, E. S., Burlakov, V. M., Goriely, A., & Snaith, H. J. (2014). Lead-free organic–inorganic tin halide perovskites for photovoltaic applications. Energy & Environmental Science, 7(9), 3061-3068.

Olaleru, S., Kirui, J., Wamwangi, D., Roro, K., & Mwakikunga, B. (2020). Perovskite solar cells: The new epoch in photovoltaics. *Solar Energy*, *196*, 295-309. https://doi.org/10.1016/j.solener.2019.12.025

Ozaki, M., Katsuki, Y., Liu, J., Handa, T., Nishikubo, R., Yakumaru, S., Hashikawa, Y., Murata, Y., Saito, T., Shimakawa, Y., Kanemitsu, Y., Saeki, A., & Wakamiya, A. (2017). Solvent-coordinated tin halide complexes as purified precursors for tin-based perovskites. *ACS Omega*, *2*(10), 7016-7021. https://doi.org/10.1021/acsomega.7b01292

Panda, N., Acharya, B., & Nayak, P. (2013). Growth and enhanced optical properties of ZnO:S nanorods and multipodes. *Materials Letters*, *100*, 257 260. https://doi.org/10.1016/j.matlet.2013.03.059

Parida, B., Singh, A., Kalathil Soopy, A. K., Sangaraju, S., Sundaray, M., Mishra, S., Liu, S. (., & Najar, A. (2022). Recent developments in Upscalable printing techniques for perovskite solar cells. *Advanced Science*, *9*(14). https://doi.org/10.1002/advs.202200308

Park, N., & Zhu, K. (2020). Scalable fabrication and coating methods for perovskite solar cells and solar modules. *Nature Reviews Materials*, *5*(5), 333-350. https://doi.org/10.1038/s41578-019-0176-2

Penner, M. H. (2017). *Basic principles of spectroscopy*. *Food Science Text Series*, 79-88. https://doi.org/10.1007/978-3-319-45776-5_6

Qiu, C., Wu, Y., Song, J., Wang, W., & Li, Z. (2022). Efficient planar perovskite solar cells with ZnO electron transport layer. *Coatings*, *12*(12), 1981. https://doi.org/10.3390/coatings12121981

Ren, G., Han, W., Deng, Y., Wu, W., Li, Z., Guo, J., Bao, H., Liu, C., & Guo, W. (2021). Strategies of modifying Spiro-ometad materials for perovskite solar cells: A review. *Journal of Materials Chemistry A*, *9*(8), 4589-4625. https://doi.org/10.1039/d0ta11564a

Roy, P., Ghosh, A., Barclay, F., Khare, A., & Cuce, E. (2022). Perovskite solar cells: A review of the recent advances. *Coatings*, *12*(8), 1089. https://doi.org/10.3390/coatings12081089

Saidi, W. A., Lee, M., Li, L., Zhou, G., & McGaughey, A. J. (2012). *Ab initio*atomistic thermodynamics study of the early stages of Cu(100) oxidation. *Physical Review B*, *86*(24). https://doi.org/10.1103/physrevb.86.245429

Savory, C. N., Walsh, A., & Scanlon, D. O. (2016). Can PB-free halide double perovskites support high-efficiency solar cells? *ACS Energy Letters*, *1*(5), 949-955. https://doi.org/10.1021/acsenergylett.6b00471

Shahbazi, M., & Wang, H. (2016). *Progress in research on the stability of organometal perovskite solar cells. Solar Energy*, *123*, 74-87. https://doi.org/10.1016/j.solener.2015.11.008

Shalan, A. E., Sharmoukh, W., Elshazly, A. N., Elnagar, M. M., Al Kiey, S. A., Rashad, M. M., & Allam, N. K. (2020). Dopant-free hole-transporting polymers for efficient, stable, and hysteresis-less perovskite solar cells. *Sustainable Materials and Technologies, 26*, e00226. https://doi.org/10.1016/j.susmat.2020.e00226

Shen, Q., Ogomi, Y., Chang, J., Toyoda, T., & Hayase, S. (2016). Bandgap Engineering and Multijunction Solar Cells with Bromine-Incorporated Tin Perovskites. The Journal of Physical Chemistry C, 120(12), 6808-6815.

Shi, X., Wu, Y., Chen, J., Cai, M., Yang, Y., Liu, X., Tao, Y., Guli, M., Ding, Y., & Dai, S. (2020). Thermally stable perovskite solar cells with an efficiency of over 21% *via* a bifunctional additive. *Journal of Materials Chemistry A*, *8*(15), 7205-7213. https://doi.org/10.1039/d0ta01255f

Snaith, H. J. (2013). Perovskites: The emergence of a new era for low-cost, high-efficiency solar cells. *The Journal of Physical Chemistry Letters, 4*(21), 3623-3630. https://doi.org/10.1021/jz4020162

Sterrer, M., & Freund, H. (2014). Properties of oxide surfaces. *Surface and Interface Science*, 229-278. https://doi.org/10.1002/9783527680559.ch15.

Stevanović, S., Stevanović, S., & Živković, R. (2022). Advantages and disadvantages of solar energy production and use. *Journal of Agricultural, Food and Environmental Sciences*, *76*(4), 65-70. https://doi.org/10.55302/jafes22764065s

Sung, S. D., Ojha, D. P., You, J. S., Lee, J., Kim, J., & Lee, W. I. (2015). 50 nm sized spherical TiO₂nanocrystals for highly efficient mesoscopic perovskite solar cells. *Nanoscale*, *7*(19), 8898-8906. https://doi.org/10.1039/c5nr01364j

Tan, K. W., Moore, D. T., Saliba, M., Sai, H., Estroff, L. A., Hanrath, T., Snaith, H. J., & Wiesner, U. (2014). Thermally induced structural evolution and performance of Mesoporous block copolymer-directed alumina perovskite solar cells. *ACS Nano*, *8*(5), 4730-4739. https://doi.org/10.1021/nn500526t

Tan, Z., Chu, Y., Chen, J., Li, J., Ji, G., Niu, G., Gao, L., Xiao, Z., & Tang, J. (2020). Lead-free perovskite variant solid solutions $Cs_2sn_{1-x}Te_xCl_6$: Bright luminescence and high anti-water stability. *Advanced Materials*, *32*(32). https://doi.org/10.1002/adma.202002443

Turkay, D., Artuk, K., Chin, X., Jacobs, D. A., Moon, S., Walter, A., Mensi, M., Andreatta, G., Blondiaux, N., Lai, H., Fu, F., Boccard, M., Jeangros, Q., Wolff, C. M., & Ballif, C. (2024). Synergetic substrate and additive engineering for over 30%-efficient perovskite-SI tandem solar cells. *Joule*, *8*(6), 1735-1753. https://doi.org/10.1016/j.joule.2024.04.015

Ukkunda, N. S., Santhoshkumar, P., Paranthaman, R., & Moses, J. (2024). *X-ray diffraction and its emerging applications in the food industry*. *Critical Reviews in Food Science and Nutrition*, 1-16. https://doi.org/10.1080/10408398.2024.2395487

Van Heerden, R., Procel, P., Mazzarella, L., Santbergen, R., & Isabella, O. (2022). *Slow shallow energy states as the origin of hysteresis in perovskite solar cells*. *Frontiers in Photonics*, *3*. https://doi.org/10.3389/fphot.2022.889837

Wang, R., Mujahid, M., Duan, Y., Wang, Z., Xue, J., & Yang, Y. (2019). A review of perovskites solar cell stability. *Advanced Functional Materials*, *29*(47). https://doi.org/10.1002/adfm.201808843

Wang, S., & Wang, S. (2015). Impacts of wind energy on environment: A review. *Renewable and Sustainable Energy Reviews*, *49*, 437-443. https://doi.org/10.1016/j.rser.2015.04.137

Wang, Y., Dar, M. I., Ono, L. K., Zhang, T., Kan, M., Li, Y., Zhang, L., Wang, X., Yang, Y., Gao, X., Qi, Y., Grätzel, M., & Zhao, Y. (2019). Thermodynamically stabilized β-cspbi ₃ –based perovskite solar cells with efficiencies >18%. *Science*, *365*(6453), 591-595. https://doi.org/10.1126/science.aav8680

Wang, Y., Zhang, Z., Lan, Y., Song, Q., Li, M., & Song, Y. (2021). Rücktitelbild: Tautomeric molecule acts as a “Sunscreen” for metal halide perovskite solar cells (Angew. Chem. 16/2021). *Angewandte Chemie*, *133*(16), 9228-9228. https://doi.org/10.1002/ange.202102311

Wei, Y., Audebert, P., Galmiche, L., Lauret, J., & Deleporte, E. (2014). Photostability of 2D organic-inorganic hybrid perovskites. *Materials*, *7*(6), 4789-4802. https://doi.org/10.3390/ma7064789

Williamson, D. F., Parker, R. A., & Kendrick, J. S. (2018). "The box plot: a simple visual method to interpret data." *Annals of Internal Medicine*, 110(11), 916-921. doi:10.7326/0003-4819-110-11-916.

Wu, C., Zhang, Q., Liu, Y., Luo, W., Guo, X., Huang, Z., Ting, H., Sun, W., Zhong, X., Wei, S., Wang, S., Chen, Z., & Xiao, L. (2018). The dawn of lead-free perovskite solar cell: Highly stable double perovskite $Cs_2AgBiBr_6$ film. *Advanced Science*, *5*(3). https://doi.org/10.1002/advs.201700759

Wu, M., Lin, Y., Chen, S., Jao, M., Chang, Y., Lee, K., Lai, C., Chen, Y., & Su, W. (2019). Achieving high-performance perovskite photovoltaic by morphology engineering of low-temperature processed zn-doped TiO_2 electron transport layer. *Small*, *16*(41). https://doi.org/10.1002/smll.202002201

Wu, S., Li, C., Lien, S. Y., & Gao, P. (2024). Temperature matters: Enhancing performance and stability of perovskite solar cells through advanced annealing methods. *Chemistry*, *6*(1), 207-236. https://doi.org/10.3390/chemistry6010010

Yang, J., Lim, E. L., Tan, L., & Wei, Z. (2022). Ink engineering in blade-coating large-area perovskite solar cells (Adv. Energy mater. 28/2022). *Advanced Energy Materials*, *12*(28). https://doi.org/10.1002/aenm.202270122

Yang, J., Sheng, W., Xiao, S., Liu, G., Lin, Z., Tan, L., & Chen, Y. (2021). Directional crystallisation by floating self-assembly for efficient and stable tin-based perovskite solar cells. *Chemistry of Materials*, *33*(12), 4362-4372. https://doi.org/10.1021/acs.chemmater.0c04906

Yang, W. S., Park, B., Jung, E. H., Jeon, N. J., Kim, Y. C., Lee, D. U., Shin, S. S., Seo, J., Kim, E. K., Noh, J. H., & Seok, S. I. (2017). Iodide management in formamidinium-lead-halide–based perovskite layers for efficient solar cells. *Science*, *356*(6345), 1376-1379. https://doi.org/10.1126/science.aan2301

Yang, Y., Liu, C., Cai, M., Liao, Y., Ding, Y., Ma, S., Liu, X., Guli, M., Dai, S., & Nazeeruddin, M. K. (2020). Dimension-controlled growth of antimony-based perovskite-like halides for lead-free and semitransparent photovoltaics. *ACS Applied Materials & Interfaces*, *12*(14), 17062-17069. https://doi.org/10.1021/acsami.0c00681

Yoo, J. J., Seo, G., Chua, M. R., Park, T. G., Lu, Y., Rotermund, F., Kim, Y., Moon, C. S., Jeon, N. J., Correa-Baena, J., Bulović, V., Shin, S. S., Bawendi, M. G., & Seo, J. (2021). Efficient perovskite solar cells via improved carrier management. *Nature*, *590*(7847), 587-593. https://doi.org/10.1038/s41586-021-03285-w

Yu, W., Wang, K., Guo, B., Qiu, X., Hao, Y., Chang, J., & Li, Y. (2017). *Effect of ultraviolet absorptivity and waterproofness of poly(3,4-ethylenedioxythiophene) with extremely weak acidity, high conductivity on enhanced stability of perovskite solar cells*. *Journal of Power Sources, 358,* 29-38. https://doi.org/10.1016/j.jpowsour.2017.05.007

Yüksel, S., Dinçer, H., Çağlayan, Ç., & Uluer, G. S. (2021). *Determining the optimal financial strategies for nuclear energy companies*. *Financial Strategies in Competitive Markets,* 1-16. https://doi.org/10.1007/978-3-030-68612-3_1

Zhang, W., Saliba, M., Moore, D. T., Pathak, S. K., Hörantner, M. T., Stergiopoulos, T., Stranks, S. D., Eperon, G. E., Alexander-Webber, J. A., Abate, A., Sadhanala, A., Yao, S., Chen, Y., Friend, R. H., Estroff, L. A., Wiesner, U., & Snaith, H. J. (2015). Ultrasmooth organic-inorganic perovskite thin-film formation and crystallisation for efficient planar heterojunction solar cells. *Nature Communications*, *6*(1). https://doi.org/10.1038/ncomms7142

Zhang, Y., Seo, S., Lim, S. Y., Kim, Y., Kim, S. G., Lee, D. K., ... & Park, N. G. (2019). Achieving reproducible and high-efficiency (> 21%) perovskite solar cells with a presynthesized FAPbI3 powder. *ACS Energy Letters*, *5*(2), 360-366.

Zhang, C., Chen, M., Fu, F., Zhu, H., Feurer, T., Tian, W., Zhu, C., Zhou, K., Jin, S., Zakeeruddin, S. M., Tiwari, A. N., Padture, N. P., Grätzel, M., & Shi, Y. (2022). CNT-based bifacial perovskite solar cells toward highly efficient 4-terminal tandem photovoltaics. *Energy & Environmental Science*, *15*(4), 1536-1544. https://doi.org/10.1039/d1ee04008a

Zheng, B., Xu, J., Ni, T., & Li, M. (2015). Geothermal energy utilization trends from a technological paradigm perspective. *Renewable Energy*, *77,* 430-441. https://doi.org/10.1016/j.renene.2014.12.035

Zheng, J., Zhang, M., Lau, C. F., Deng, X., Kim, J., Ma, Q., Chen, C., Green, M. A., Huang, S., & Ho-Baillie, A. W. (2017). Spin-coating free fabrication for highly efficient perovskite solar cells. *Solar Energy Materials and Solar Cells*, *168,* 165-171. https://doi.org/10.1016/j.solmat.2017.04.029

Zhong, Y., Hufnagel, M., Thelakkat, M., Li, C., & Huettner, S. (2020). Role of PCBM in the suppression of hysteresis in perovskite solar cells. *Advanced Functional Materials*, *30*(23). https://doi.org/10.1002/adfm.201908920

Zhong, Z., Hasnah, M., Broadbent, A., Dooryhee, E., & Lucas, M. (2019). Phase-space matching between bent Laue and flat Bragg crystals. *Journal of Synchrotron Radiation*, *26*(6), 1917-1923. https://doi.org/10.1107/s1600577519010774

Zhou, D., Zhou, T., Tian, Y., Zhu, X., & Tu, Y. (2018). Perovskite-based solar cells: Materials, methods, and future perspectives. *Journal of Nanomaterials, 2018,* 1-15.

Zhu, H., Liu, Y., Eickemeyer, F. T., Pan, L., Ren, D., Ruiz-Preciado, M. A., Carlsen, B., Yang, B., Dong, X., Wang, Z., Liu, H., Wang, S., Zakeeruddin, S. M., Hagfeldt, A., Dar, M. I., Li, X., & Grätzel, M. (2020). Tailored Amphiphilic molecular mitigators for stable perovskite solar cells with 23.5% efficiency. *Advanced Materials*, *32*(12). https://doi.org/10.1002/adma.201907757

APPENDICES

Appendix A: Publication

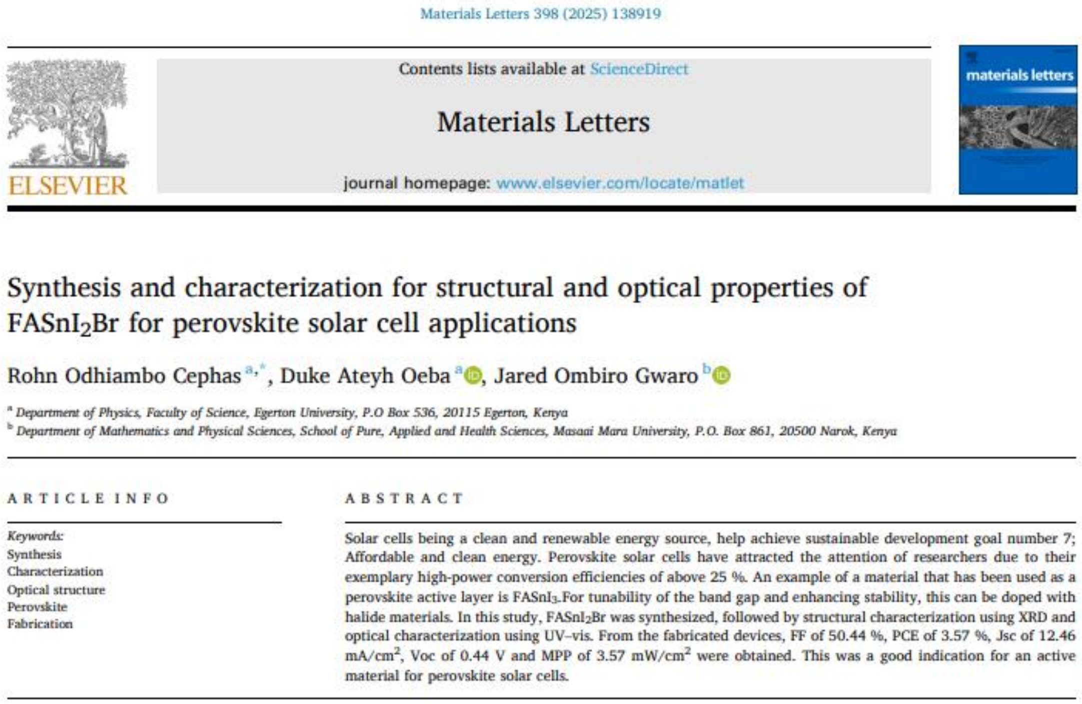

Materials Letters 398 (2025) 138919

Contents lists available at ScienceDirect

Materials Letters

journal homepage: www.elsevier.com/locate/matlet

Synthesis and characterization for structural and optical properties of $FASnI_2Br$ for perovskite solar cell applications

Rohn Odhiambo Cephas [a,*], Duke Ateyh Oeba [a], Jared Ombiro Gwaro [b]

[a] *Department of Physics, Faculty of Science, Egerton University, P.O Box 536, 20115 Egerton, Kenya*

[b] *Department of Mathematics and Physical Sciences, School of Pure, Applied and Health Sciences, Masaai Mara University, P.O. Box 861, 20500 Narok, Kenya*

ARTICLE INFO

Keywords:
Synthesis
Characterization
Optical structure
Perovskite
Fabrication

ABSTRACT

Solar cells being a clean and renewable energy source, help achieve sustainable development goal number 7; Affordable and clean energy. Perovskite solar cells have attracted the attention of researchers due to their exemplary high-power conversion efficiencies of above 25 %. An example of a material that has been used as a perovskite active layer is $FASnI_3$.For tunability of the band gap and enhancing stability, this can be doped with halide materials. In this study, $FASnI_2Br$ was synthesized, followed by structural characterization using XRD and optical characterization using UV–vis. From the fabricated devices, FF of 50.44 %, PCE of 3.57 %, Jsc of 12.46 mA/cm^2, Voc of 0.44 V and MPP of 3.57 mW/cm^2 were obtained. This was a good indication for an active material for perovskite solar cells.

Appendix B: Research Permit

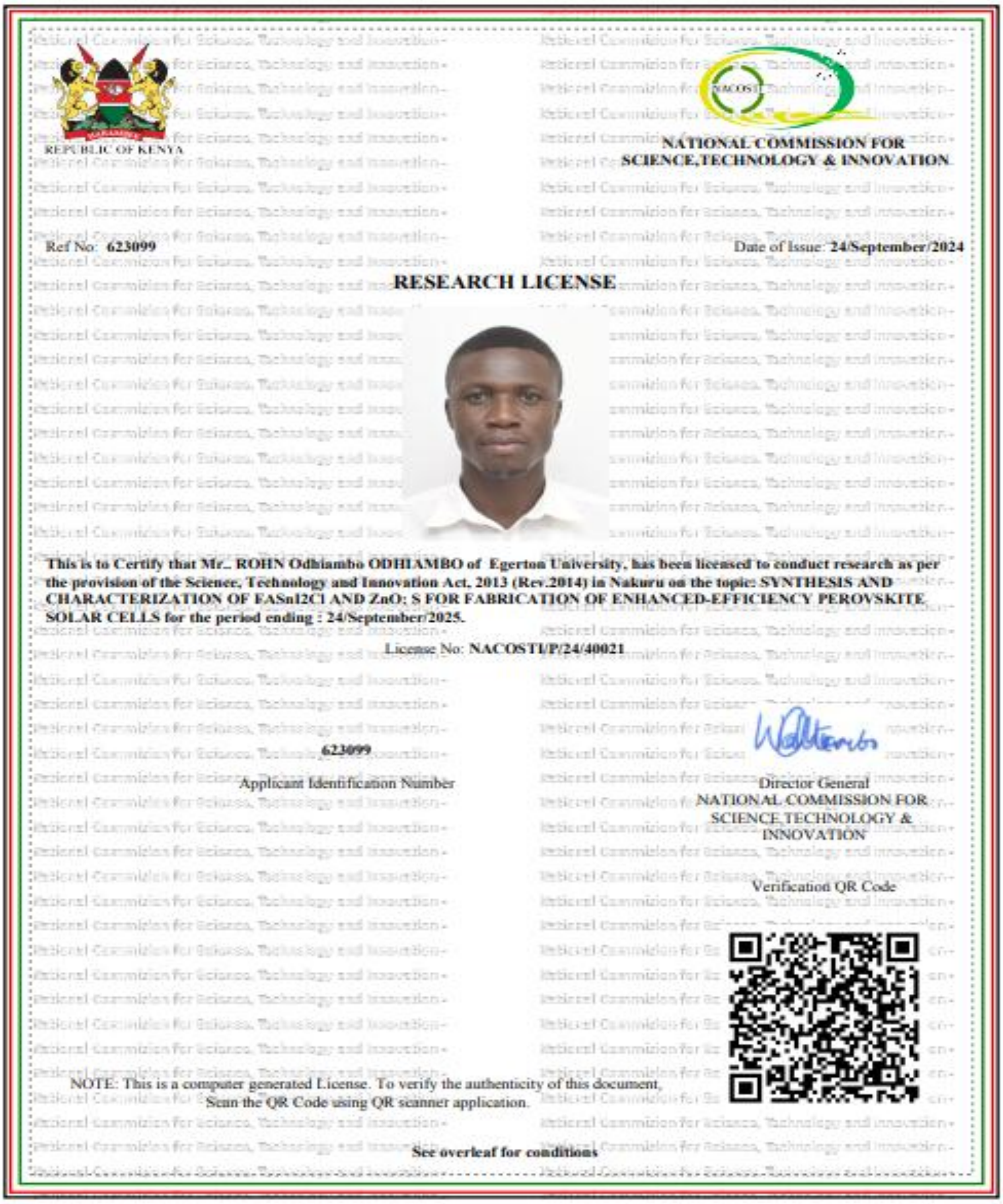

REPUBLIC OF KENYA

NATIONAL COMMISSION FOR SCIENCE,TECHNOLOGY & INNOVATION

Ref No: **623099**

Date of Issue: **24/September/2024**

RESEARCH LICENSE

This is to Certify that Mr.. ROHN Odhiambo ODHIAMBO of Egerton University, has been licensed to conduct research as per the provision of the Science, Technology and Innovation Act, 2013 (Rev.2014) in Nakuru on the topic: SYNTHESIS AND CHARACTERIZATION OF FASnI2Cl AND ZnO: S FOR FABRICATION OF ENHANCED-EFFICIENCY PEROVSKITE SOLAR CELLS for the period ending : 24/September/2025.

License No: **NACOSTI/P/24/40021**

623099
Applicant Identification Number

Director General
NATIONAL COMMISSION FOR
SCIENCE,TECHNOLOGY &
INNOVATION

Verification QR Code

NOTE: This is a computer generated License. To verify the authenticity of this document,
Scan the QR Code using QR scanner application.

See overleaf for conditions